



Article

# Simply Prepared Magnesium Vanadium Oxides as Cathode Materials for Rechargeable Aqueous Magnesium Ion Batteries

Milica M. Vasić<sup>1</sup>, Miloš Milović<sup>2</sup> , Danica Bajuk-Bogdanović<sup>1</sup> , Tamara Petrović<sup>1</sup> and Milica J. Vujković<sup>1,\*</sup><sup>1</sup> Faculty of Physical Chemistry, University of Belgrade, Studentski trg 12-16, 11000 Belgrade, Serbia<sup>2</sup> Institute of Technical Sciences of SASA, Knez Mihajlova 35/IV, 11000 Belgrade, Serbia

\* Correspondence: milica.vujkovic@ffh.bg.ac.rs

**Abstract:** Vanadium-oxide-based materials exist with various vanadium oxidation states having rich chemistry and ability to form layered structures. These properties make them suitable for different applications, including energy conversion and storage. Magnesium vanadium oxide materials obtained using simple preparation route were studied as potential cathodes for rechargeable aqueous magnesium ion batteries. Structural characterization of the synthesized materials was performed using XRD and vibrational spectroscopy techniques (FTIR and Raman spectroscopy). Electrochemical behavior of the materials, observed by cyclic voltammetry, was further explained by BVS calculations. Sluggish Mg<sup>2+</sup> ion kinetics in MgV<sub>2</sub>O<sub>6</sub> was shown as a result of poor electronic and ionic wiring. Complex redox behavior of the studied materials is dependent on phase composition and metal ion inserted/deinserted into/from the material. Among the studied magnesium vanadium oxides, the multiphase oxide systems exhibited better Mg<sup>2+</sup> insertion/deinsertion performances than the single-phase ones. Carbon addition was found to be an effective dual strategy for enhancing the charge storage behavior of MgV<sub>2</sub>O<sub>6</sub>.



**Citation:** Vasić, M.M.; Milović, M.; Bajuk-Bogdanović, D.; Petrović, T.; Vujković, M.J. Simply Prepared Magnesium Vanadium Oxides as Cathode Materials for Rechargeable Aqueous Magnesium Ion Batteries. *Nanomaterials* **2022**, *12*, 2767. <https://doi.org/10.3390/nano12162767>

Academic Editor: Jipeng Cheng

Received: 19 July 2022

Accepted: 5 August 2022

Published: 12 August 2022

**Publisher's Note:** MDPI stays neutral with regard to jurisdictional claims in published maps and institutional affiliations.



**Copyright:** © 2022 by the authors. Licensee MDPI, Basel, Switzerland. This article is an open access article distributed under the terms and conditions of the Creative Commons Attribution (CC BY) license (<https://creativecommons.org/licenses/by/4.0/>).

**Keywords:** magnesium vanadium oxides; rechargeable magnesium batteries; aqueous electrolyte; cyclic voltammetry; charge storage improvement

## 1. Introduction

Today, lithium-ion batteries are used in numerous electronic devices and electric vehicles because of their stable cycle life, light weight, and high capacity [1,2]. In spite of this, limited lithium resources, relatively high costs, and operational safety problems bring their future massive application into question [3–5]. Therefore, considerable research efforts have been devoted towards development of alternative battery systems [5–12], based on Earth's abundant elements such as Na [6,13], Mg [5], Al [7,10,14], Zn [8], etc. Challenging concepts such as solid-state [13] and aqueous rechargeable battery systems [15,16] have been developed to achieve safe and sustainable energy storage technology. Rechargeable magnesium (RMBs), sodium (RSBs), and aluminum (RABs) are considered very promising candidates for partial replacement of the lithium-ion batteries, due to high natural abundance of elements (Mg, Na, and Al) and resulting lower costs of these batteries than the Li ones, and their better atmospheric stability, safety of handling, and eco-friendliness [5,9,17,18]. Regarding Na and Al storage systems, critical issues have been successfully addressed [13,14] with the aim to design materials and interfaces for their practical application.

The choice of host material for the storage of Mg<sup>2+</sup> is of huge importance for the development of RMBs. Layered intercalation materials offer advantages of relatively high capacity and good structural stability, while the ion intercalation is allowed by their large interlayer space [5,19,20]. Vanadium oxides have been attracting attention as layered materials potentially applicable for RMBs since the first publication about the ability of V<sub>2</sub>O<sub>5</sub> to reversibly electrochemically intercalate Mg<sup>2+</sup> at room temperature [17]. Transportation of Mg<sup>2+</sup> ions in α-V<sub>2</sub>O<sub>5</sub> phase is often slow because of strong interactions between Mg<sup>2+</sup>

and neighboring O atoms [5,21]. However, defect engineering (ionic vacancy, doping, amorphous phases, and phase interfaces) and solvation effects may facilitate diffusion of bivalent ions [22,23]. Furthermore, density functional theory investigation revealed that, by increasing magnesium intercalation concentration,  $\alpha$ -phase  $V_2O_5$  host material can be converted into  $\epsilon$  and  $\delta$  phase [24]. So far, different vanadium-oxide-based materials have been synthesized and tested as possible cathodes for RMBs [5,18,22,25–29]. Various preparation methods have been used for that purpose, including hydrothermal or solvothermal synthesis, usage of microwave irradiation, conventional heat-treatment, sol–gel method, etc. [30–35].

The advantages of the use of aqueous electrolytes over nonaqueous ones in the first place include lower toxicity, flammability, environmental risks, and costs [8,36,37], while improved  $Mg^{2+}$  kinetics is also expected in oxide cathodes [17,18,38,39]. In general, the kinetics of multivalent ions is more difficult than the kinetics of alkaline ions due to the stronger interaction of multivalent ions with structural and electrolyte surrounding. On the other hand, double and triple charge can provide higher charge transfer, while the co-intercalated water can protect multivalent ions from strong interaction with the surrounding environment [40], thus making structure more stable during cycling. Recently, great success has been achieved with Zn and Al aqueous electrochemistry [15,16], while similar achievements seem to be still elusive for Ca and Mg aqueous chemistry. Nevertheless, Mg-ion aqueous batteries may provide certain advantages over Zn and Al aqueous systems, in terms of the cyclic stability. For example, better cyclic stability of the sodium vanadate cathode has been demonstrated in Mg- than in Al-containing aqueous electrolytes [41], as a result of weaker interaction of bare  $Mg^{2+}$  than  $Al^{3+}$  ion with the structure and different pH of the electrolyte. Further, Mg-ion aqueous chemistry does not suffer from dendrite issues as is the case with Zn-aqueous ion batteries.

A number of studies have been published on rechargeable aqueous batteries containing vanadium-oxide-based cathode materials [42–50], pointing out the importance of appropriate choice of electrode structure for battery performances. In this work, several Mg-V-O materials synthesized by simple preparation route were studied and discussed as potential cathodes for aqueous RMBs. Addition of carbon to the Mg-V-O was considered as a strategy for the charge storage improvement.

## 2. Experimental Part

For the synthesis of the MgVO-HT material (composition  $MgV_2O_6$ ), MgVO precursor was prepared by precipitation method [51,52], using  $NH_4VO_3$  and  $Mg(OH)_2$  reactants mixed at the Mg:V molar ratio 1:2. Namely,  $NH_4VO_3$  was dissolved in 1 wt.%  $NH_4OH$  solution to make 0.5 M  $NH_4VO_3$ , which was subsequently mixed with the appropriate amount of  $Mg(OH)_2$ . The mixture was evaporated to dryness with stirring, and then dried at 100 °C. The obtained precursor was ground in an agate mortar, and finally calcined in air at 550 °C (sample denoted as MgVO-LT) or successively at 550 and 700 °C (denoted as MgVO-HT), for 12 h at each temperature.

MgVO materials of the compositions  $Mg_2V_2O_7$  and  $Mg_3V_2O_8$ , prepared for comparison purposes, were made in a manner analogous to that of the MgVO-HT, but with the reactants ratio appropriate to the desired compositions, and final calcination temperature of 800 °C in the case of  $Mg_3V_2O_8$ .

To obtain MgVO material with improved electrochemical properties, 100 mg of MgVO-HT material was mixed with 31 mg of sucrose, and the mixture was thermally treated at 700 °C for 2 h under Ar atmosphere. The material prepared in this way was named MgVO/C.

X-ray diffraction measurements (XRD) were performed using Philips PW 1050 X-ray powder diffractometer, in Bragg–Brentano focusing geometry, with Ni-filtered  $Cu K\alpha$  radiation. For the analysis of the XRD patterns, ICSD database [53] was used. Crystallite size of  $MgV_2O_6$  phase was estimated applying Scherrer equation [54] to the peak positioned at 14.3° (2 $\theta$ ).

Scanning Electron Microscopy (SEM) measurements were performed by means of the SEM device Phenom ProX.

Fourier transform infrared spectra (FTIR) were collected using a Thermo Scientific IS20 Nicolet device, with the KBr technique. The measurements were carried out with 32 scans per spectrum and  $4\text{ cm}^{-1}$ -resolution. Raman spectroscopy was performed with a Thermo Scientific DXR Raman microscope, using an excitation wavelength of 532 nm and power of 8 mW. The measurements included 10 exposures per spectrum, 10 s exposure time, and pinhole size of 50  $\mu\text{m}$ . The objective magnification was  $10\times$ . For the UV-Vis spectroscopic measurements, Thermo Scientific Evolution 220 UV-Visible Spectrophotometer was employed.

Electrochemical measurements were carried out in a three-electrode cell, with a Gamry PCI4/300 potentiostat/galvanostat. Saturated calomel electrode (SCE) was used as a reference electrode, and a platinum foil as a counter electrode. Working electrodes were prepared by depositing a paste consisting of active material, Vulcan carbon black, and poly(vinylidene fluoride) (PVDF) (2 wt.% PVDF in N-methyl-2-pyrrolidone) at the weight ratio 85:10:5 onto the glassy carbon rods, and drying the rods under vacuum overnight. All the measurements were performed in aqueous solutions of nitrate salts (Mg, Al, or Li) at room temperature. The values of specific current presented in the paper are given relative to the weight of active material.

For the insight of possible  $\text{Mg}^{2+}$  diffusion pathways in the structures of interest, the bond valence method has been utilized. Bond valence sum (BVS) calculations were carried out in 3DBVSMAPPER [55] software. The method is based on the valence sum rule and includes calculation of bond valence sum value for the chosen ion (in this case,  $\text{Mg}^{2+}$ ) located at the particular point in the crystal by measuring distances to the neighboring counter-ions (in this case,  $\text{O}^{2-}$ ) [56]. Assuming that any point in the unit cell with the BVS value for  $\text{Mg}^{2+}$  close to 2 represents a possible location of  $\text{Mg}^{2+}$  to appear there, the BVS distribution on a 3D grid reveals possible locations of  $\text{Mg}^{2+}$  occurrence in the lattice. By obtaining volume for a given BVS mismatch (in our case,  $2 \pm 0.1$  valence units), the method is readily used for visualizing a 3D map of diffusion pathways of some particular ion [55].

### 3. Results and Discussion

#### 3.1. Structural Characterization

Structural characterization of the MgVO precursor was performed before and after thermal treatments by means of XRD and vibrational spectroscopy techniques (FTIR and Raman spectroscopy). According to the XRD results, the nonthermally treated precursor is a mixture composed of  $\text{Mg}(\text{OH})_2$  and  $\text{NH}_4\text{VO}_3$  phases (Figure 1a). After 12 h annealing at  $550\text{ }^\circ\text{C}$  in air, the precursor phases were transformed into the composite material containing  $\text{V}_2\text{O}_5$ ,  $\text{MgV}_2\text{O}_6$ , and  $\text{Mg}_2\text{V}_2\text{O}_7$  phases with the weight fractions 31%, 51%, and 18%, respectively, designated as MgVO-LT (Figure 1b). Finally, after further annealing of the MgVO-LT at  $700\text{ }^\circ\text{C}$  for 12 h in air, the single-phase material consisting of  $\text{MgV}_2\text{O}_6$  phase is obtained (Figure 1c) and named MgVO-HT.

Vibrational spectroscopy analysis yielded results consistent with those obtained using the XRD analysis. The vibrational band of water, i.e., humidity of the samples, is observed at around  $1635\text{ cm}^{-1}$  in the FTIR spectra of all the samples, resulting from O-H-O scissoring vibrations [57]. Characteristic modes of  $\text{MgV}_2\text{O}_6$  phase [58–63] can be seen in the FTIR and Raman spectra of both MgVO-LT and MgVO-HT samples (Figure 2). Besides those of  $\text{MgV}_2\text{O}_6$ , vibrational modes of  $\text{V}_2\text{O}_5$  and  $\text{Mg}_2\text{V}_2\text{O}_7$  phases [58–63] can be recognized in the FTIR and Raman spectra of the MgVO-LT, as assigned in Figure 2 and Tables 1 and 2. For the mentioned phases, stretching  $\text{V}=\text{O}$  vibrational modes can be found in the region  $920\text{--}1030\text{ cm}^{-1}$ , while the stretching asymmetric  $\text{VO}_4$  and  $\text{VO}_6$  ones can be seen in the wavenumber range  $815\text{--}920\text{ cm}^{-1}$  (Figure 2). Spectral bands in the regions  $620\text{--}740\text{ cm}^{-1}$  and  $520\text{--}580\text{ cm}^{-1}$  can be associated with the stretching asymmetric and symmetric V-O-V vibrations, respectively. The bending symmetric  $\text{VO}_4$  and  $\text{VO}_6$  vibrational modes can be found in the region  $410\text{--}450\text{ cm}^{-1}$ . Detailed assignation of individual bands of the Mg-V-O

phases is presented in Tables 1 and 2. Vibrational modes of the  $\text{NH}_4\text{VO}_3$  dominate the spectra of the precursor material, (Table S1, Supplementary Materials). In the Raman spectra, the high-frequency  $\text{MgV}_2\text{O}_6$  modes ( $205$  and  $150\text{ cm}^{-1}$ ) become slightly shifted in the vanadate mixture (for a few  $\text{cm}^{-1}$  towards higher frequencies), as a result of the interaction with other phases and coupling of their modes.

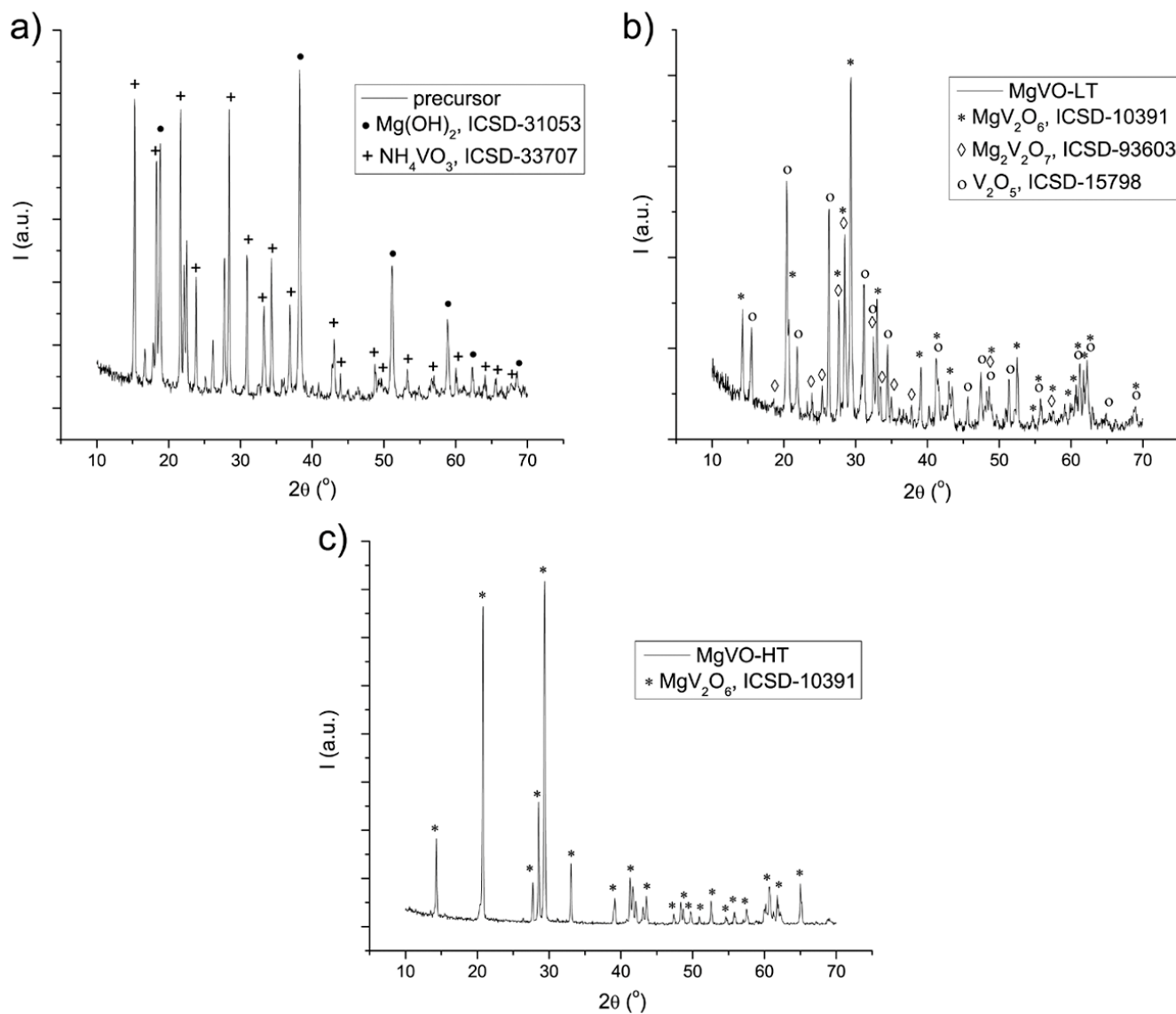


**Figure 1.** XRD patterns of the MgVO precursor (a); MgVO-LT (b); and MgVO-HT (c) material.

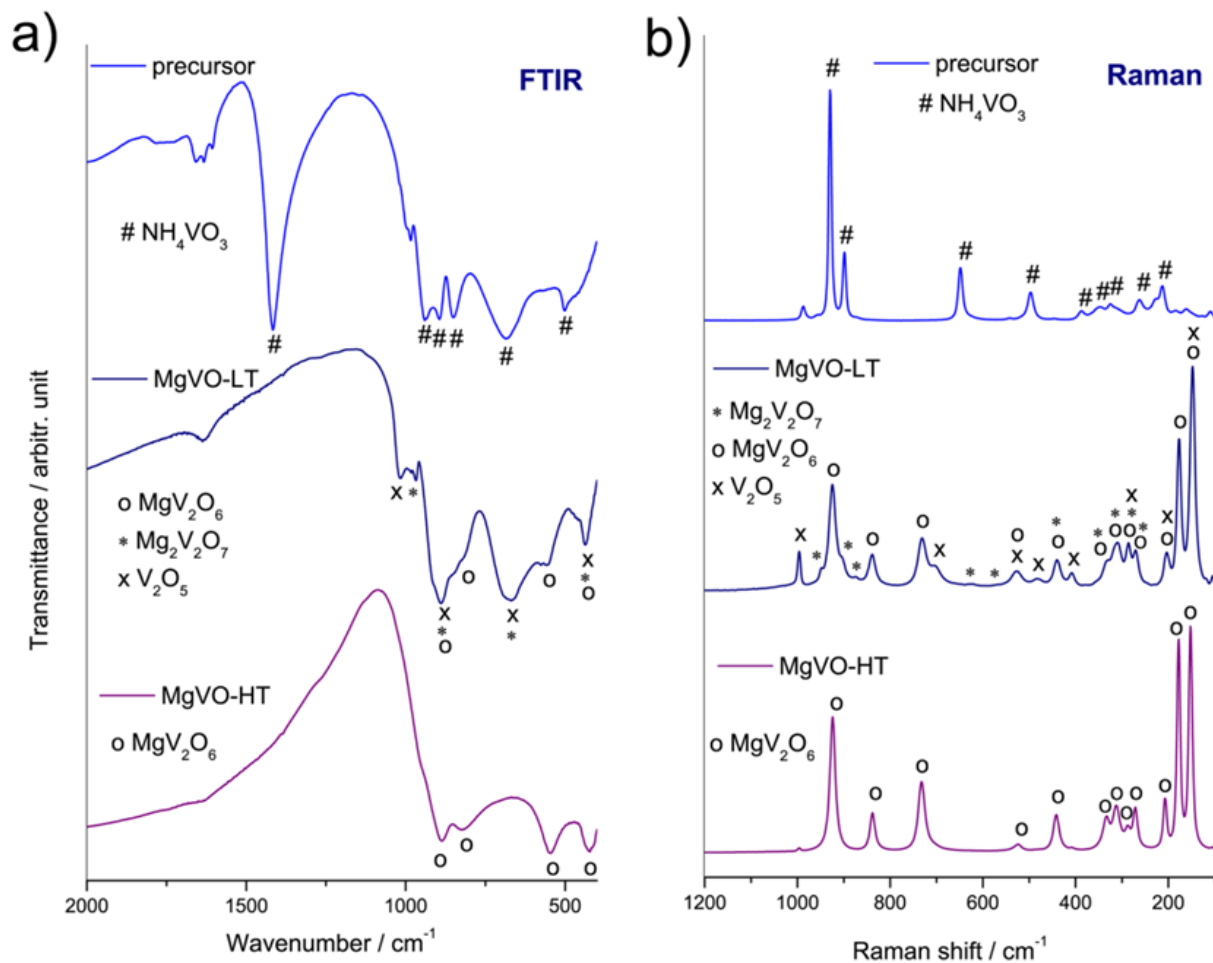


**Figure 2.** FTIR (a) and Raman (b) spectra of the MgVO precursor, MgVO-LT, and MgVO-HT material.

**Table 1.** Assignment of the FTIR and Raman spectral bands of the MgVO-HT material.

Band Position	Assignment	Reference
FTIR spectra		
885 and 815 cm <sup>-1</sup>	MgV <sub>2</sub> O <sub>6</sub> -stretching asymmetric $\nu_{as}(\text{VO}_4)$ and $\nu_{as}(\text{VO}_6)$	[58,63]
540 cm <sup>-1</sup>	MgV <sub>2</sub> O <sub>6</sub> -stretching symmetric $\nu_s(\text{VOV})$	[58]
425 cm <sup>-1</sup>	MgV <sub>2</sub> O <sub>6</sub> -bending symmetric $\delta_s(\text{VO}_4)$ and $\delta_s(\text{VO}_6)$ ; and Mg-O vibrations	[58,63]
Raman spectra		
925 cm <sup>-1</sup>	MgV <sub>2</sub> O <sub>6</sub> -stretching $\nu(\text{V}=\text{O})$ and $\nu_s(\text{VO}_4)$ (symmetric)	[58]
840 cm <sup>-1</sup>	MgV <sub>2</sub> O <sub>6</sub> -stretching asymmetric $\nu_{as}(\text{VO}_4)$ and $\nu_{as}(\text{VO}_6)$	[58]
733 cm <sup>-1</sup>	MgV <sub>2</sub> O <sub>6</sub> -stretching asymmetric $\nu_{as}(\text{VOV})$	[58]
524 cm <sup>-1</sup>	MgV <sub>2</sub> O <sub>6</sub> -stretching symmetric $\nu_s(\text{VOV})$	[58]
444 cm <sup>-1</sup>	MgV <sub>2</sub> O <sub>6</sub> -bending symmetric $\delta_s(\text{VO}_4)$ and $\delta_s(\text{VO}_6)$	[58]
270–330 cm <sup>-1</sup>	MgV <sub>2</sub> O <sub>6</sub> -bending asymmetric $\delta_{as}(\text{VO}_4)$ and $\delta_{as}(\text{VO}_6)$	[58,61]
205 cm <sup>-1</sup> ; 175 cm <sup>-1</sup> ; 150 cm <sup>-1</sup>	MgV <sub>2</sub> O <sub>6</sub>	[59,61]

### 3.2. Morphological Characterization

SEM measurements of MgVO-LT and MgVO-HT samples (Figure 3) clearly confirm their morphological difference, which occurs as a result of the applied annealing temperature and the formed phase composition. At first glance, MgVO-LT microparticles (10–20  $\mu\text{m}$ ) are composed of irregular loose nanospherical particles (Figure 3, up). Still, a certain part of them remained undecorated (visibly better in Figure S1 (left)). The observed nanoparticles' looseness is favorable for easy diffusion of electrolyte ions. If we look closely,

there are also some nanowires in the sample, visibly better at larger magnifications (Figure S1, right). It seems there are more nanowires in the bulk; so, they need more time to be activated during cycling. Three types of MgVO-LT particles can be correlated with the appearance of three phases in MgO-LT sample, as identified by XRD. The formation of a pure  $\text{MgV}_2\text{O}_6$  phase upon increasing temperature completely changes the morphology of the sample. Large microagglomerates (5–20  $\mu\text{m}$ ) without a defined nanostructure dominate the morphology of MgVO-LT sample.

**Table 2.** Assignment of the FTIR and Raman spectral bands of the MgVO-LT material.

Band Position	Assignment	Reference
FTIR spectra		
1020 $\text{cm}^{-1}$	$\text{V}_2\text{O}_5$ -stretching $\nu(\text{V}-\text{O})$	[58]
975 $\text{cm}^{-1}$	$\text{Mg}_2\text{V}_2\text{O}_7$ -stretching $\nu(\text{V}^{\text{V}}=\text{O})$ and $\nu_s(\text{VO}_4)$ (symmetric)	[58]
815–920 $\text{cm}^{-1}$	$\text{V}_2\text{O}_5$ , $\text{MgV}_2\text{O}_6$ , and $\text{Mg}_2\text{V}_2\text{O}_7$ -stretching asymmetric $\nu_{\text{as}}(\text{VO}_4)$ and $\nu_{\text{as}}(\text{VO}_6)$	[58]
620–720 $\text{cm}^{-1}$	$\text{V}_2\text{O}_5$ and $\text{Mg}_2\text{V}_2\text{O}_7$ -stretching asymmetric $\nu_{\text{as}}(\text{VOV})$	[58,60,61]
540 $\text{cm}^{-1}$	$\text{MgV}_2\text{O}_6$ -stretching symmetric $\nu_s(\text{VOV})$	[58]
420–450 $\text{cm}^{-1}$	$\text{V}_2\text{O}_5$ , $\text{MgV}_2\text{O}_6$ , and $\text{Mg}_2\text{V}_2\text{O}_7$ -bending symmetric $\delta_s(\text{VO}_4)$ and $\delta_s(\text{VO}_6)$	[58]
Raman spectra		
996 $\text{cm}^{-1}$	$\text{V}_2\text{O}_5$ -stretching $\nu(\text{V}^{\text{V}}=\text{O})$ and $\nu_s(\text{VO}_4)$ (symmetric)	[58]
922 $\text{cm}^{-1}$	$\text{MgV}_2\text{O}_6$ -stretching $\nu(\text{V}^{\text{V}}=\text{O})$ and $\nu_s(\text{VO}_4)$ (symmetric)	[58,59]
840 $\text{cm}^{-1}$	$\text{V}_2\text{O}_5$ and $\text{MgV}_2\text{O}_6$ -stretching asymmetric $\nu_{\text{as}}(\text{VO}_4)$ and $\nu_{\text{as}}(\text{VO}_6)$ ; $\text{Mg}_2\text{V}_2\text{O}_7$ -stretching asymmetric $\nu_{\text{as}}(\text{VOV})$	[58]
730 $\text{cm}^{-1}$	$\text{V}_2\text{O}_5$ and $\text{MgV}_2\text{O}_6$ -stretching asymmetric $\nu_{\text{as}}(\text{VOV})$	[58,59]
523 $\text{cm}^{-1}$	$\text{MgV}_2\text{O}_6$ and $\text{Mg}_2\text{V}_2\text{O}_7$ -stretching symmetric $\nu_s(\text{VOV})$	[58,59]
440 $\text{cm}^{-1}$	$\text{MgV}_2\text{O}_6$ and $\text{Mg}_2\text{V}_2\text{O}_7$ -bending symmetric $\delta_s(\text{VO}_4)$ and $\delta_s(\text{VO}_6)$	[58]
412 $\text{cm}^{-1}$	$\text{V}_2\text{O}_5$ -bending symmetric $\delta_s(\text{VO}_4)$ and $\delta_s(\text{VO}_6)$	[58,59]
335 $\text{cm}^{-1}$	$\text{V}_2\text{O}_5$ and $\text{Mg}_2\text{V}_2\text{O}_7$ -bending asymmetric $\delta_{\text{as}}(\text{VO}_4)$ and $\delta_{\text{as}}(\text{VO}_6)$	[58]
310 $\text{cm}^{-1}$	$\text{MgV}_2\text{O}_6$ and $\text{Mg}_2\text{V}_2\text{O}_7$ -bending asymmetric $\delta_{\text{as}}(\text{VO}_4)$ and $\delta_{\text{as}}(\text{VO}_6)$	[58]
285 $\text{cm}^{-1}$	$\text{Mg}_2\text{V}_2\text{O}_7$ -bending asymmetric $\delta_{\text{as}}(\text{VO}_4)$ and $\delta_{\text{as}}(\text{VO}_6)$	[58]
272 $\text{cm}^{-1}$	$\text{MgV}_2\text{O}_6$ -bending asymmetric $\delta_{\text{as}}(\text{VO}_4)$ and $\delta_{\text{as}}(\text{VO}_6)$	[58]
205 $\text{cm}^{-1}$ ; 175 $\text{cm}^{-1}$ ; 150 $\text{cm}^{-1}$	$\text{MgV}_2\text{O}_6$	[59,61]

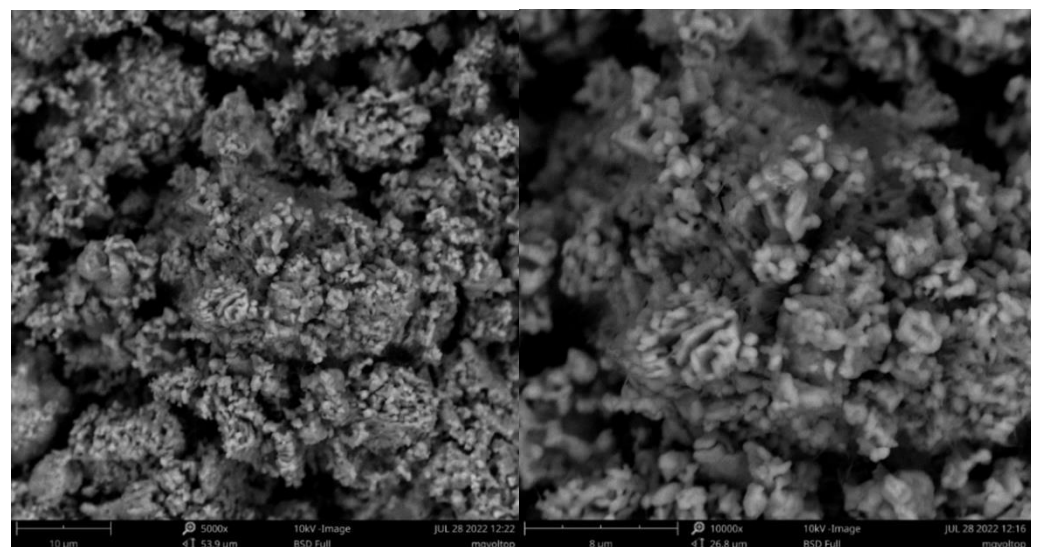


**Figure 3.** Cont.

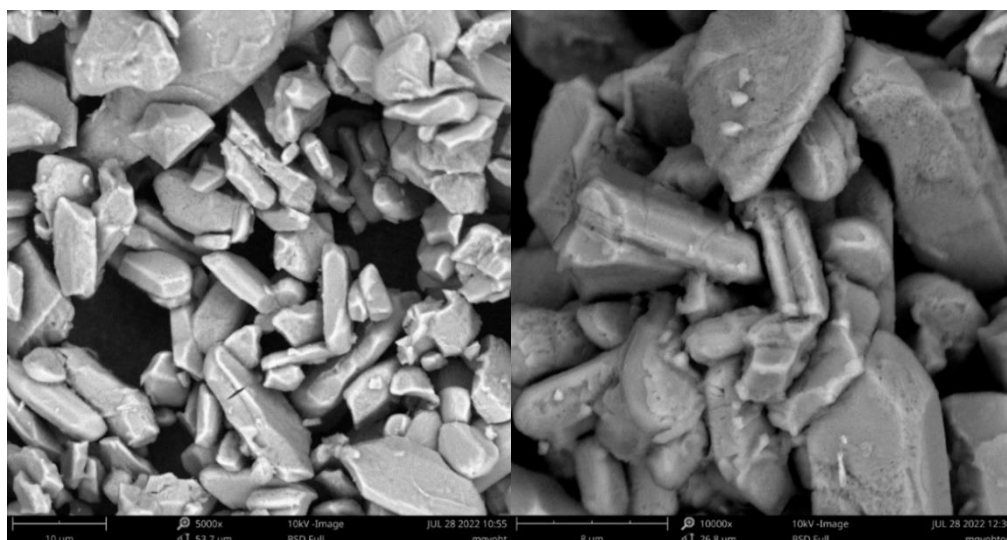


Figure 3. SEM micrographs of MgVO-LT (up) and MgVO-HT (down).

Based on the morphological observations, the polyphase material ( $V_2O_5/MgV_2O_6/Mg_2V_2O_7$ ) is expected to show better diffusion behavior than single-phase  $MgV_2O_6$  material, which will be investigated in the following sections.

### 3.3. Electrochemical Characterization

#### 3.3.1. MgVO-HT Material

Since the simply prepared MgVO-HT is a single-phase material, its electrochemical properties are discussed first, followed by an examination of the MgVO-LT material. Cyclic voltammetric (CV) characterization of the MgVO-HT material in 3M  $Mg(NO_3)_2$  solution revealed three poorly defined redox pairs (Figure 4a), resulting from the insertion/deinsertion of  $Mg^{2+}$  ions at different structural sites, including changes in the vanadium valence state [18]. By repeating CV measurements, current values were shown to be unstable. Quite low current values were obtained, which can be attributed to the low electrical conductivity of the sample.

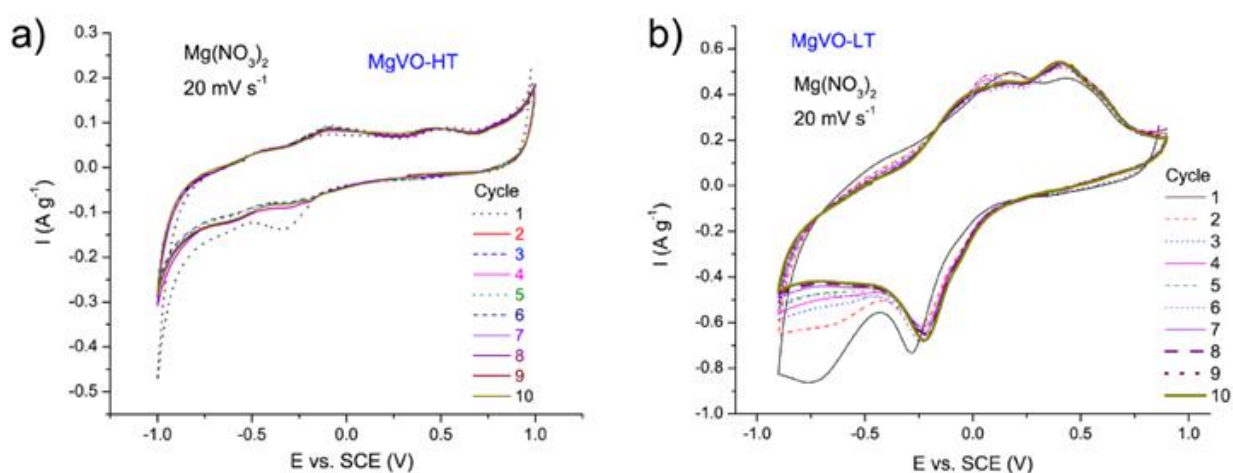
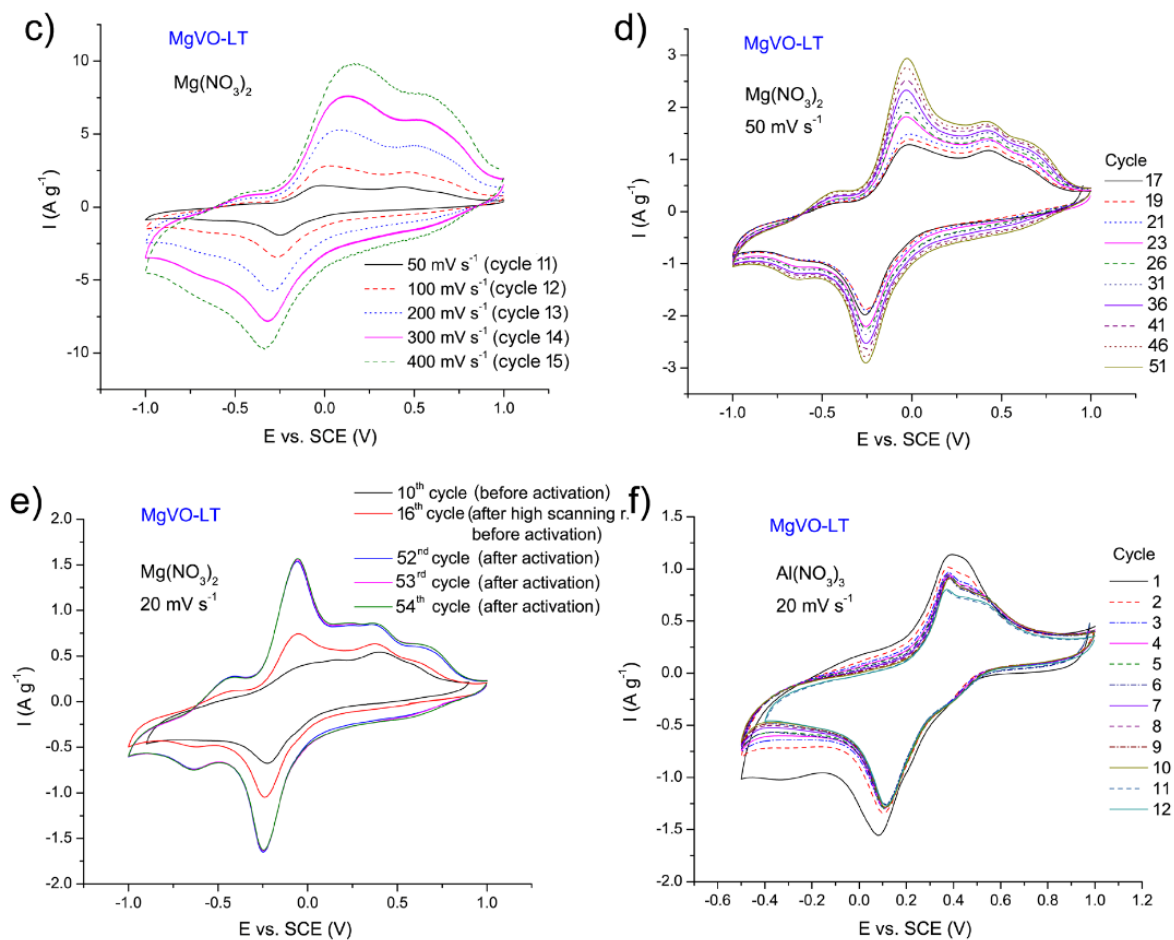


Figure 4. Cont.



**Figure 4.** Cyclic voltammograms of MgVO-HT in 3M  $\text{Mg}(\text{NO}_3)_2$  at  $20 \text{ mV s}^{-1}$  (a); MgVO-LT in 3M  $\text{Mg}(\text{NO}_3)_2$  at  $20 \text{ mV s}^{-1}$  (b) and at higher scanning rates (c) before activation; activation of the MgVO-LT in 3M  $\text{Mg}(\text{NO}_3)_2$  at  $50 \text{ mV s}^{-1}$  (d); MgVO-LT in 3M  $\text{Mg}(\text{NO}_3)_2$  at  $20 \text{ mV s}^{-1}$  before and after activation (e); MgVO-LT in 1M  $\text{Al}(\text{NO}_3)_3$  at  $20 \text{ mV s}^{-1}$  (f).

### 3.3.2. MgVO-LT Material

The subject of further analyses was the multiphase composite MgVO-LT material. According to the electrochemical test in 3M  $\text{Mg}(\text{NO}_3)_2$ , performed by recording CVs at  $20 \text{ mV s}^{-1}$ , the current became stabilized after 7 cycles (Figure 4b). CVs at higher scanning rates retained the shape of those at  $20 \text{ mV s}^{-1}$  (Figure 4c). An additional scan at  $20 \text{ mV s}^{-1}$ , conducted in order to check the electrochemical performance after scanning at higher rates, revealed an unexpected increase in current values (Figure 4e). Then, further activation was performed by repeated cycling at  $50 \text{ mV s}^{-1}$  up to the stabilization (35 cycles) (Figure 4d), after which successive scans at  $20 \text{ mV s}^{-1}$  demonstrated stable current values (Figure 4e). The activation including growth of current values up to the stabilization is a result of water molecules entering the structure of the MgVO-LT [8]. Although not very high, maximal current values observed for the composite MgVO-LT material were more than 10 times higher than those obtained for simply prepared pure  $\text{MgV}_2\text{O}_6$  phase (Figure 4a,e).

Positions of the cathodic peaks of the MgVO-LT, as well as of MgVO-HT, around  $-0.20$  and  $-0.62 \text{ V vs. SCE}$  (at  $20 \text{ mV s}^{-1}$ ), correspond to those published in the literature for the  $\text{V}_2\text{O}_5$  xerogel/graphite composite in the saturated aqueous solution of  $\text{Mg}(\text{NO}_3)_2$  [40], suggesting that, in the studied materials, the  $\text{Mg}^{2+}$  ions were electrochemically inserted at the sites equivalent to those published for the mentioned  $\text{V}_2\text{O}_5$  composite [40]. This would mean that inserted  $\text{Mg}^{2+}$  ions occupied the sites in the structure near the center of square-planar oxygen atoms, as well as those around apical oxygen atoms [40,64]. In the anodic direction, the peak at around  $-0.43 \text{ V}$  coincides with that of the aforementioned



literature [40], but this is not the case at potentials more positive than  $-0.20$  V, where the shape of the CV curves and peak positions differ from those from [40] (Figure 4). This suggests that the main  $Mg^{2+}$  extraction process from MgVO-LT is faster when compared to  $V_2O_5$ -based xerogel (the less positive main anodic peak) due to higher crystallinity of oxides in the mixture and different  $Mg^{2+}$ -ion surroundings.

Additional testing of the MgVO-LT material was carried out in 1M  $Al(NO_3)_3$  by recording CVs at  $20$  mV  $s^{-1}$  (Figure 4f). In this case, the observed redox peaks correspond to the insertion/deinsertion of  $Al^{3+}$  ions into/from the vanadium oxide mixture. Unlike in the  $Mg(NO_3)_2$  solution, pronounced decline in the current values was observed with each subsequent CV cycle recorded in the  $Al(NO_3)_3$  electrolyte (Figure 4f), suggesting damage of the electrode material with the electrochemical treatment. This resulted from mechanical strain in the structure growing with the progress of the insertion process [28] and was also contributed by the higher acidity of the  $Al(NO_3)_3$  than the  $Mg(NO_3)_2$  solution. Anyway, the maximal current values observed for the MgVO-LT material in  $Al(NO_3)_3$  solution were lower than those in  $Mg(NO_3)_2$ , but significantly higher than the current values reached for the MgVO-HT in the  $Al(NO_3)_3$  solution of the same concentration (Figures 4f and S2, Supplementary Materials).

### 3.4. Characterization of the MgVO-LT Material after Electrochemical Treatment

For a deeper insight into the behavior of the MgVO-LT material in the studied electrolytes, further examinations were performed. FTIR spectroscopy analysis of the working electrodes MgVO-LT after electrochemical measurements revealed certain changes in the vibrational bands of the electrode material, as a consequence of the electrochemical treatments in the  $Mg(NO_3)_2$  and  $Al(NO_3)_3$  electrolytes (Figure 5a). UV-Vis absorption spectra of the electrolytes previously used in the electrochemical measurements exhibited a peak only at around 300 nm, which corresponds to the presence of nitrate ions [65], for both  $100\times$  diluted electrolytes and undiluted  $Mg(NO_3)_2$  (Figure 5b,c). However, an additional absorption band in the range 350–500 nm can be observed in the UV-Vis spectrum of undiluted  $Al(NO_3)_3$  electrolyte, which can be related with the presence of dissolved vanadium (V) species in the electrolyte [66–68], confirming degradation of the electrode material during the electrochemical measurements in  $Al(NO_3)_3$  electrolyte.

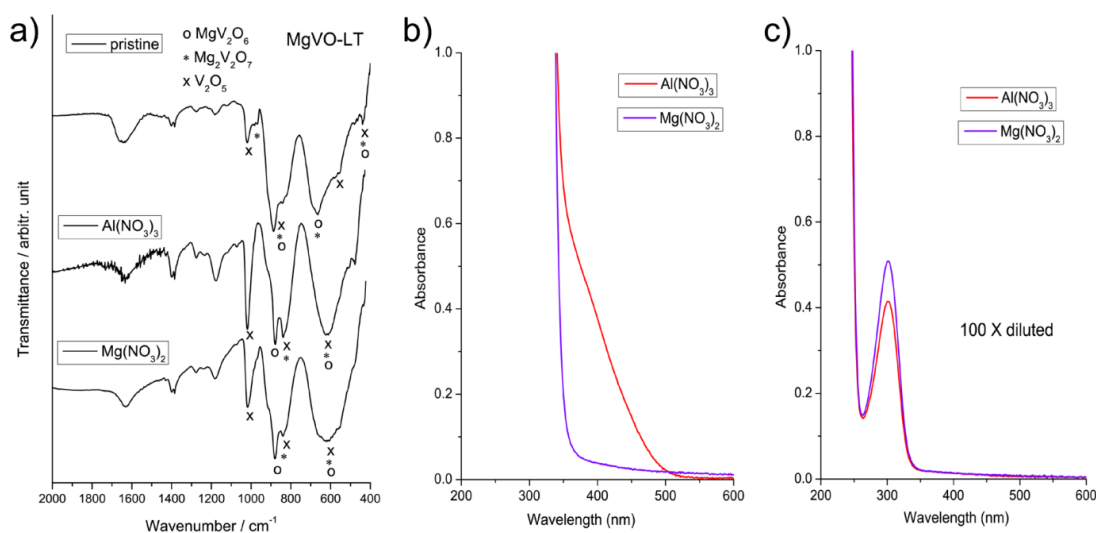


**Figure 5.** FTIR spectra of the MgVO-LT working electrodes before and after electrochemical measurements in  $Mg(NO_3)_2$  and  $Al(NO_3)_3$  electrolytes (a); UV-Vis absorption spectra of the  $Mg(NO_3)_2$  and  $Al(NO_3)_3$  electrolytes without dilution (b) and  $100\times$  diluted (c), after electrochemical measurements with MgVO-LT electrodes.

Comparison of the FTIR spectra of the electrode paste before and after electrochemical measurements showed, after the measurements, an increase in the vibrational band of  $V_2O_5$  at  $1020\text{ cm}^{-1}$  (stretching  $\nu(\text{V-O})$  [58]) relative to the vibrational bands of  $MgV_2O_6$  and  $Mg_2V_2O_7$  (Figure 5a), suggesting partial degradation of the  $MgV_2O_6$  and  $Mg_2V_2O_7$  phases during the electrochemical treatments in  $Mg(\text{NO}_3)_2$  and  $Al(\text{NO}_3)_3$ . The peak at  $975\text{ cm}^{-1}$ , resulting from stretching  $\nu(\text{V}^{\text{V}}=\text{O})$  and  $\nu_s(\text{VO}_4)$  (symmetric) vibrations of  $Mg_2V_2O_7$  [58], disappeared in the spectra after the treatments, especially in the case of Al-redox process. Further, instead of merged peaks at  $815\text{--}920\text{ cm}^{-1}$  corresponding to the vibrations of all three phases, observed in the as-prepared electrode paste, two separate peaks at around  $880$  and  $830\text{ cm}^{-1}$  appeared in the spectrum after the electrochemical experiments (Figure 5a). This peaks can be ascribed to the stretching asymmetric  $\nu_{as}(\text{VO}_4)$  and  $\nu_{as}(\text{VO}_6)$  vibrations of the  $MgV_2O_6$  and  $V_2O_5$  phases [58], respectively. Most probably, the separation of the peaks resulted from weakening of the stretching asymmetric vibrational bands of the  $Mg_2V_2O_7$  phase, which were expected to appear at around  $873$  and  $850\text{ cm}^{-1}$ , as a consequence of partial deficiency of this phase in the electrode paste after the electrochemical treatments. These indicators of partial degradation of the electrode material were more pronounced for the  $Al(\text{NO}_3)_3$  than for the  $Mg(\text{NO}_3)_2$  electrolyte (Figure 5a). Structural stability of the  $V_2O_5$  phase was probably improved due to insertion of the metal ions within the  $V_2O_5$  structure during the electrochemical experiments [69] and introduction of hydroxyl groups at the oxide surface [41]. Broadening of the vibrational bands in the range  $500\text{--}720\text{ cm}^{-1}$  after electrochemical measurements could be a consequence of certain structural distortions in the phases present in the electrode material, including changes in the interlayer distances [70], resulting from the  $Mg^{2+}$  or  $Al^{3+}$  ion insertion into their structures. The results of the Raman spectroscopy of the electrochemically treated samples are in agreement with the findings obtained from the FTIR analysis, (Figure S3, Supplementary Materials), but do not offer unambiguous conclusions, because of phase heterogeneity of the samples and dependence of micro-Raman spectra appearance on the sites in the samples chosen for the analysis.

#### Bond Valence Sum (BVS) Calculations for the Phases Present in the MgVO-HT and MgVO-LT

Let us explain redox behavior of the vanadate mixture from the aspect of the bond valence method (BVS), which helps obtain insight into possible  $Mg^{2+}$  diffusion pathways of the examined vanadium oxide structures. In our study, crystallographic data of  $MgV_2O_6$  (monoclinic s. g.  $C2/m$  [71]),  $V_2O_5$  (orthorhombic s. g.  $Pmmm$  [72]), and  $Mg_2V_2O_7$  (monoclinic s. g.  $P2_1/c$  [73]) have been used as input for BVS calculation and its results are presented in Figure 6.

In  $MgV_2O_6$ , magnesium occupies  $2/m$  octahedral Mg1 sites between  $VO_n$  layers [71], thus forming chains of edge-sharing octahedra  $VO_6$  along b-direction (Figure 6a). Although this seems the most obvious path for  $Mg^{2+}$  ion diffusion, there is no continuous network of BVS isosurfaces (Figure 6b). Therefore,  $Mg^{2+}$  ion migration within this structure is inherently hindered to a considerable degree, providing only low current densities, as confirmed by electrochemical measurements.

In alpha  $Mg_2V_2O_7$  structure, magnesium occupies two crystallographic positions, Mg1 and Mg2, also in octahedral coordination and forms zig-zag chains of edge-sharing  $Mg1O_6$  and  $Mg2O_6$  octahedra alternating along c-direction (Figure 6c). Both positions Mg1 and Mg2, however, remain completely isolated from the rest of the isosurface area (Figure 6d), rendering this structure more/less inactive for reversible magnesium extraction. This is in agreement with the results of cyclic voltammetric characterization of the  $Mg_2V_2O_7$  material, given in Figure S4a (Supplementary Materials).

In contrast to  $MgV_2O_6$  and  $Mg_2V_2O_7$ , which provide only limited capabilities for  $Mg^{2+}$  ion transfer, the alpha  $V_2O_5$  structure offers two solid intercrossed channels for  $Mg^{2+}$  diffusion along the c- and b-axis, as displayed in Figure 6e,f. In this manner, a continuous network is formed for unobstructed 2D migration of  $Mg^{2+}$  within this structure. The observation is in accordance with the cyclic voltammetry measurements, which

evidence substantially higher currents obtained for the MgVO-LT sample (composite of abovementioned phases) than MgVO-HT (which is plain  $\text{MgV}_2\text{O}_6$ ).

On the other hand, the contribution of Mg vanadate phases to the redox activity of the MgVO-LT cannot be neglected. The electrolyte remained colorless upon cycling of vanadate mixtures in  $\text{Mg}(\text{NO}_3)_2$ , which indicates a certain degree of structural arrangement/conversion of Mg-vanadate phases during cycling and possible synergy among vanadate phases in the mixed oxide. More pronounced electrochemical activity of the  $\text{MgV}_2\text{O}_6$  phase towards insertion/deinsertion of  $\text{Mg}^{2+}$  and  $\text{Al}^{3+}$  ions in the MgVO-LT than in the sample with the pure  $\text{MgV}_2\text{O}_6$  phase could result from the smaller crystal dimensions (45 nm crystallite size of  $\text{MgV}_2\text{O}_6$  in MgVO-LT, instead of 57 nm in MgVO-HT) and particle size, but also indicates that some kind of synergistic effect among different phases present in the MgVO-LT composite is possible during the electrochemical processes, which would make performance of the multiphase composite better than those of individual phases, similarly to the catalytic activity of Mg-V-O materials [74].

This may be caused by the presence of oxygen vacancies and grain boundaries. Generated oxygen vacancies in multiphase material can shorten the path for  $\text{Mg}^{2+}$  ions (acting as channels for their diffusion) and/or improve the electronic wiring by changing the electronic cloud (induced by free electrons generated around vacancies) [22]. Besides, the phase boundary may help diffusion of  $\text{Mg}^{2+}$  ions [22], thus introducing defects and/or active sites [22,75]).

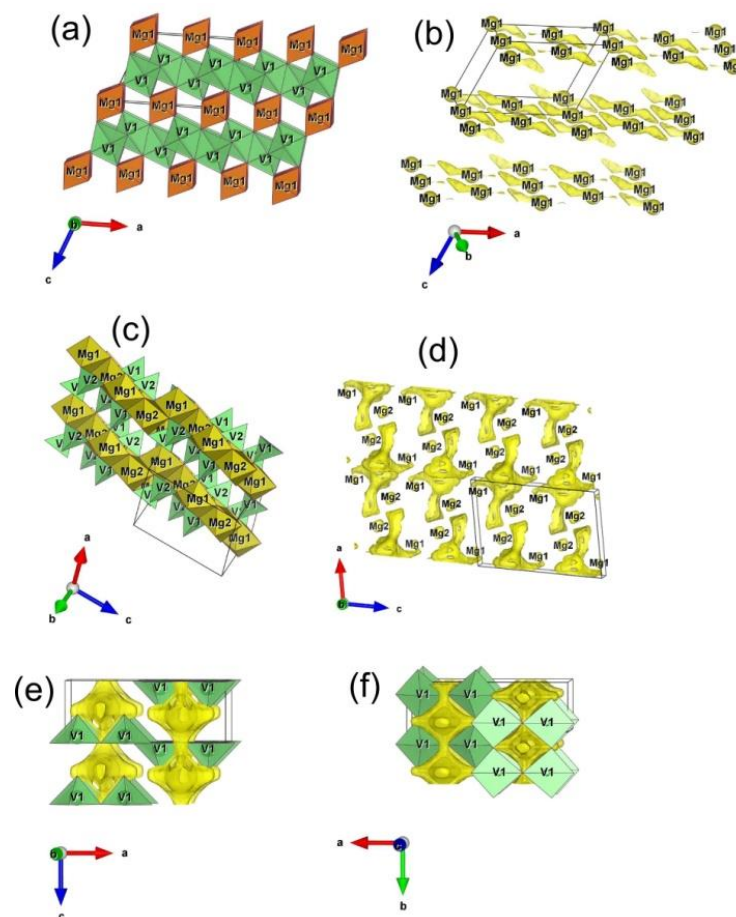


**Figure 6.** Models of migration pathways for  $\text{Mg}^{2+}$  ion obtained by BVS analysis of the phase constituents of MgVO-LT. Polyhedral representation of  $\text{Mg}_2\text{VO}_6$  (a) and BVS map within its structure (b). Polyhedral representation of  $\alpha\text{-Mg}_2\text{V}_2\text{O}_7$  (c) and BVS map within its structure (d). View on c- (e) and d-channels (f) within  $\alpha\text{-V}_2\text{O}_5$ . BVS volumes are defined by  $\pm 0.1$  v.u. mismatch from the valence +2 of Mg.

### 3.5. Structural, Morphological, and Electrochemical Characterization of the MgVO/C Material with Improved Performances

Taking into account poor redox kinetics of MgVO-HT (or  $\text{MgV}_2\text{O}_6$ ), caused by low electronic and ionic wiring, the further step was directed towards the charge storage improvement of this phase. With this aim, carbon was incorporated into the MgVO-HT by mixing the material with sucrose and annealing the mixture at 700 °C for 2 h under Ar atmosphere, thus obtaining the material marked as MgVO/C.

Structural analysis of the prepared composite powder revealed that the material changed the phase composition after thermal treatment with sucrose (Figure 7). The presence of  $\text{MgV}_3\text{O}_8$ ,  $\text{Mg}_3\text{V}_2\text{O}_8$ , and  $\text{MgV}_2\text{O}_4$  crystalline phases in the sample, with weight fractions (without C) 54%, 35%, and 11%, respectively, is observed. The sucrose addition also changes the morphology of sample (Figure 8). Plate microagglomerates ( $\sim 10 \mu\text{m}$ ) were retained upon carbon formation, but their surface became more porous and rougher. As can be seen from Figure 8, MgVO/C agglomerates are composed from irregular nano- and microparticles, formed as a consequence of the carbon reduction treatment. This indicates not only improved electronic conductivity but also enhanced diffusion behavior.

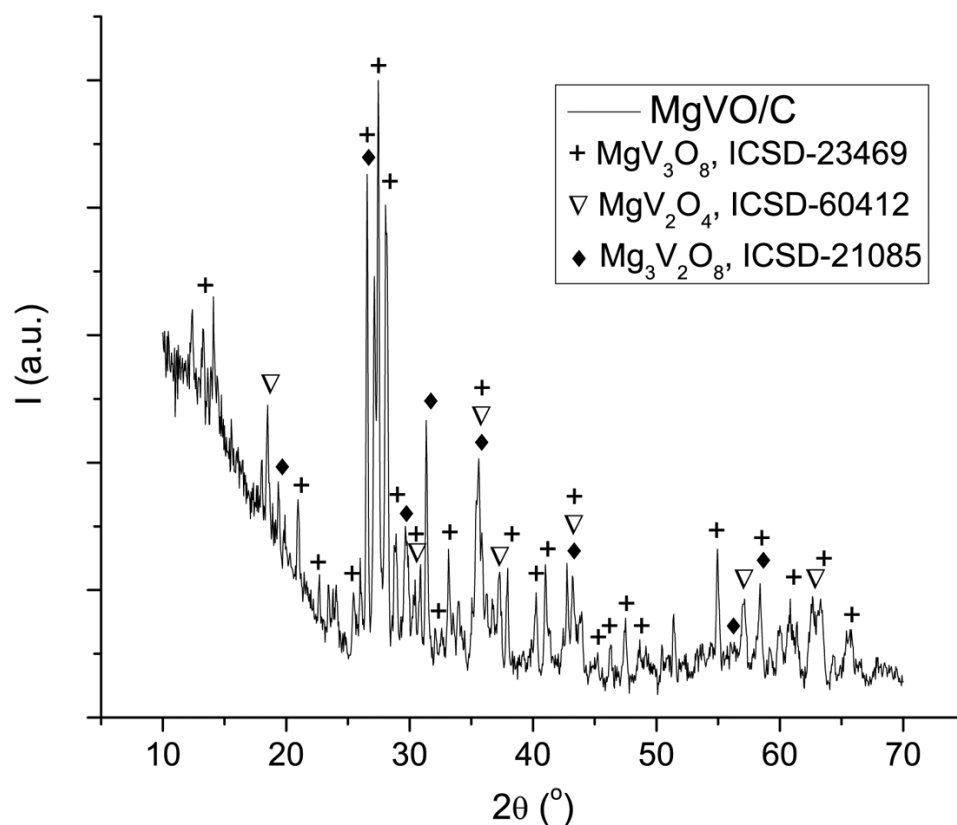
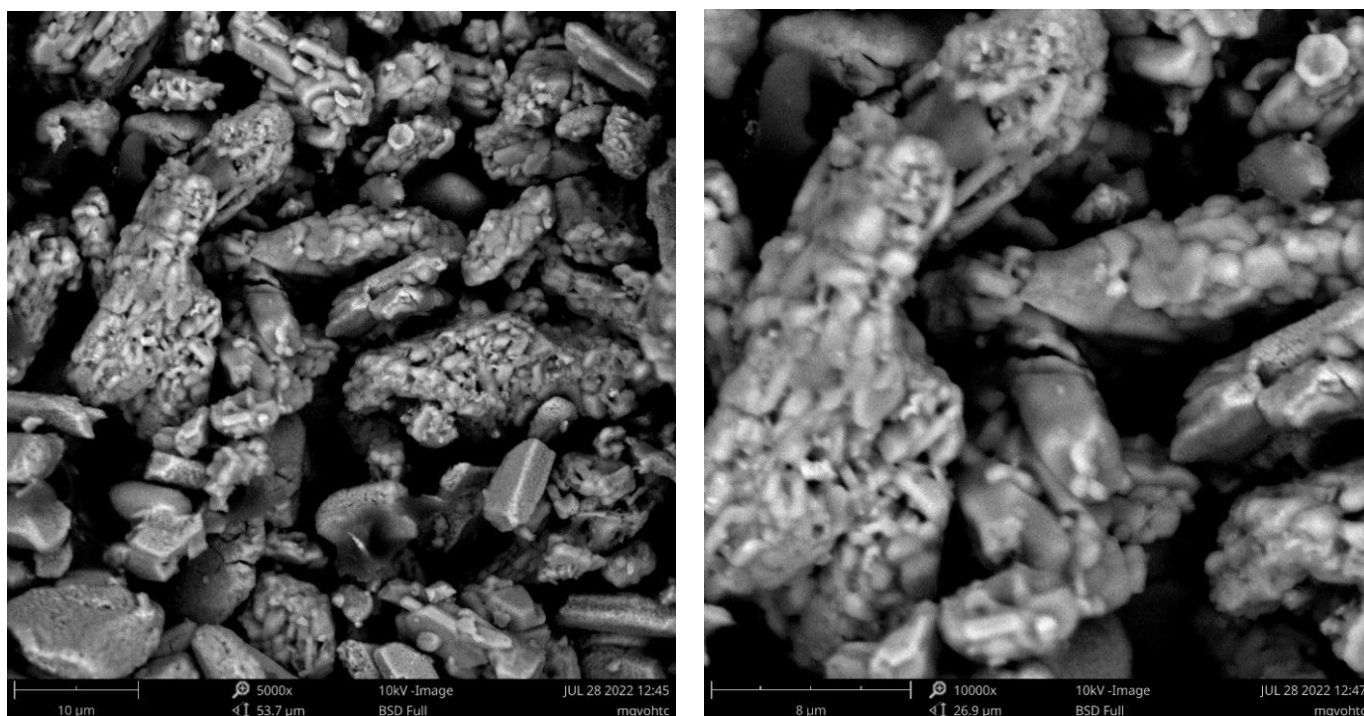
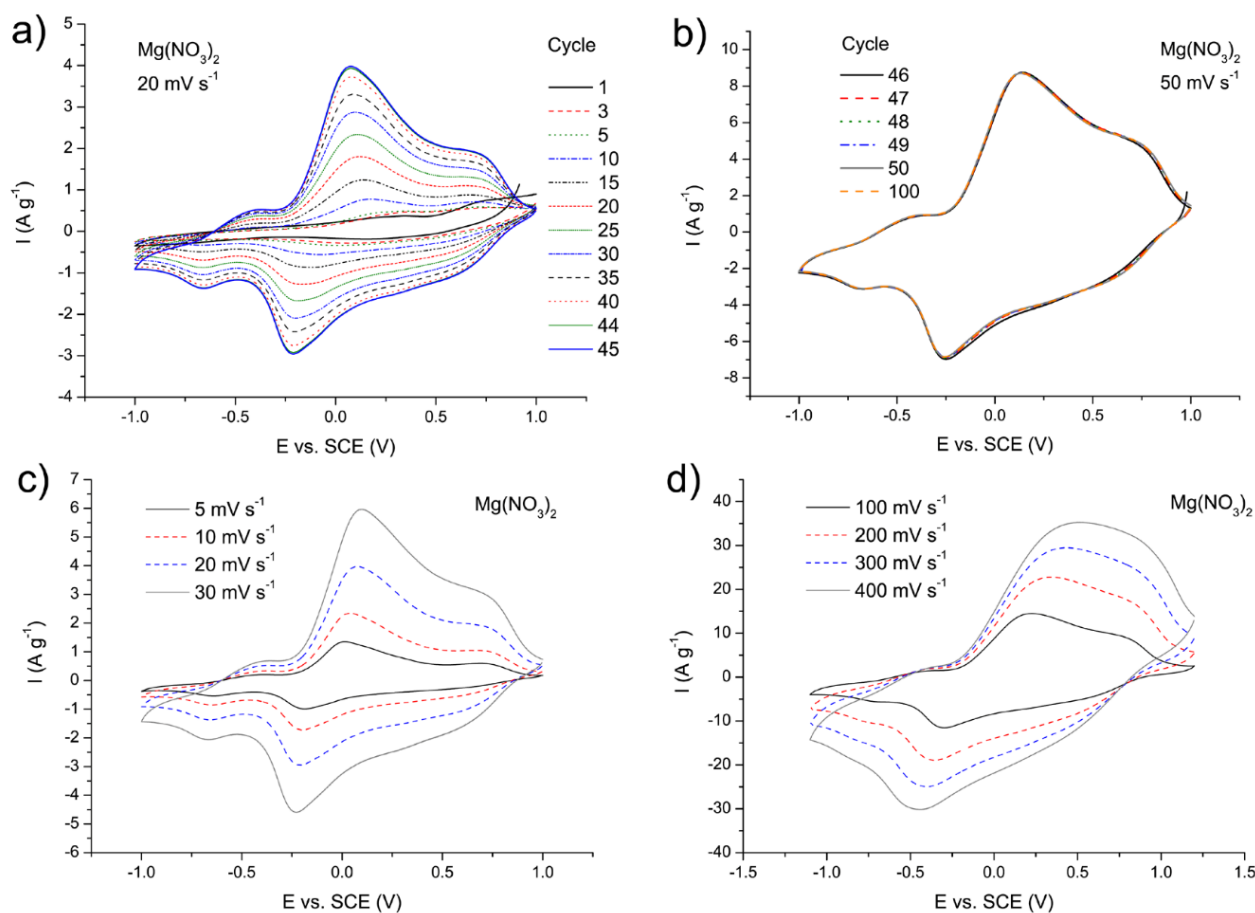


Figure 7. XRD patterns of the MgVO/C material.



**Figure 8.** SEM micrographs of MgVO/C at different magnifications.

Electrochemical test of the MgVO/C in 3M  $\text{Mg}(\text{NO}_3)_2$  solution performed by cyclic voltammetry measurements at  $20 \text{ mV s}^{-1}$  showed the presence of redox peaks (Figure 9a), which correspond to valence state transition of vanadium together with insertion/deinsertion of  $\text{Mg}^{2+}$  into/from the structure of the MgVO/C [18]. Increase in the current values including further activation of the material was observed with each subsequent measurement cycle, up to the 45th cycle, when the current became stabilized (Figure 9a). The maximal current after stabilization is around 40 times higher than that of the MgVO-HT, and twice as high as that of the MgVO-LT material (Figures 4a,e and 9a). Cyclic voltammograms (5 cycles) recorded afterwards at  $50 \text{ mV s}^{-1}$  with the same working electrode confirmed the stability of the host material during  $\text{Mg}^{2+}$  insertion/deinsertion (Figure 9b). Gradual activation of the material (CVs at  $20 \text{ mV s}^{-1}$ ), similarly to the MgVO-LT, probably resulted from coininsertion of water molecules into the structure of MgVO/C, together with  $\text{Mg}^{2+}$  ions, due to which the high charge density of  $\text{Mg}^{2+}$  became buffered [8], allowing faster cation transfer. Similarly to the previously described materials MgVO-HT and MgVO-LT, redox peak positions of MgVO/C indicate that inserted  $\text{Mg}^{2+}$  ions occupied the sites in the structure near the center of square-planar oxygen atoms and around apical oxygen atoms [40]. Cyclic voltammograms recorded at lower and higher scanning rates revealed well-defined redox peaks up to the scanning rate of  $100 \text{ mV s}^{-1}$  (Figure 9c,d), suggesting the ability of the material to tolerate relatively high currents. However, at scanning rates higher than  $100 \text{ mV s}^{-1}$ , individual peaks in both directions became merged, since the  $\text{Mg}^{2+}$  ions did not have enough time to completely extract from and insert into the material within the used potential range, causing irreversible behavior.



**Figure 9.** Cyclic voltammograms of the MgVO/C recorded in 3M  $\text{Mg}(\text{NO}_3)_2$  solution: at  $20 \text{ mV s}^{-1}$  (a); at  $50 \text{ mV s}^{-1}$  after 45 successive cycles previously recorded at  $20 \text{ mV s}^{-1}$  using the same working electrode (b); at  $5\text{--}30 \text{ mV s}^{-1}$  (c); at  $100\text{--}400 \text{ mV s}^{-1}$  (d).

The  $\text{MgV}_3\text{O}_8$  phase, present as the most abundant phase of the MgVO/C material, is significant for the electrochemical activity of the sample towards insertion/deinsertion of  $\text{Mg}^{2+}$  ions. This phase is characterized by the mixed valence ( $\text{V}^{5+}/\text{V}^{4+}$ ), which is considered to optimize electron conductivity and give various redox sites for the electrochemical process [76]. Further, the  $\text{MgV}_2\text{O}_4$  phase, although present in minor amounts, is supposed to have complex defect chemistry, including the presence of some  $\text{V}^{5+}/\text{V}^{4+}$  beside the  $\text{V}^{3+}$  in the material [28], which additionally contributed to the electrochemical activity of the studied material. Thus, in spite of the fact that 35% of the MgVO/C sample is an inactive phase ( $\text{Mg}_3\text{V}_2\text{O}_8$ , Figure S4b (Supplementary Materials)), the MgVO/C exhibited improved electrochemical activity towards insertion/deinsertion of  $\text{Mg}^{2+}$  ions compared with other simply prepared Mg-V-O materials studied in this work.

After stabilization, chronopotentiometric curves were recorded. The voltage-capacity profile exhibits two waves (Figure 10), which suggests the multistep  $\text{Mg}^{2+}$  ion insertion behavior [29]. Specific capacity of around  $50 \text{ mAh g}^{-1}$  was reached at  $0.91 \text{ A g}^{-1}$ . Subsequent charge/discharge curves are very similar. Still, the capacity is inferior when compared with the values of some reported vanadium oxides [40,41,77–79] measured in Mg-containing aqueous electrolytes (Table S2).

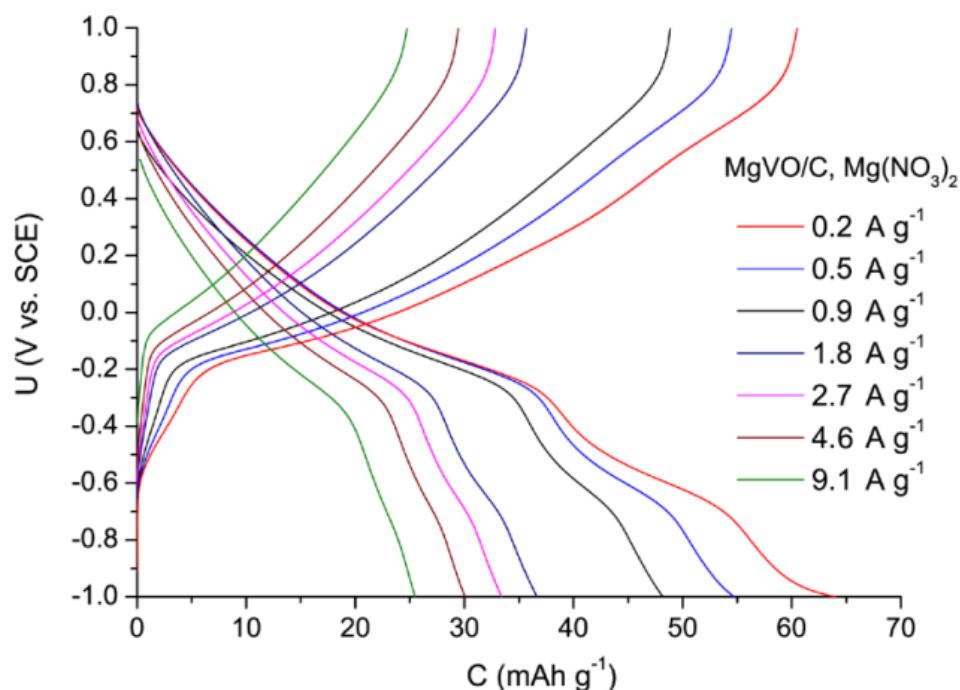


**Figure 10.** Chronopotentiometric curves of the MgVO/C in 3M Mg(NO<sub>3</sub>)<sub>2</sub>, recorded at different current values.

### 3.5.1. BVS Calculations for the Phases Present in the MgVO/C

Further explanation of the electrochemical behavior of the MgVO/C was given from the point of view of possible Mg<sup>2+</sup> diffusion pathways in the structures of interest, utilizing the bond valence method. In the presented study, crystallographic data of Mg<sub>3</sub>V<sub>2</sub>O<sub>8</sub> (orthorhombic s.g. *Cmca* [80]), MgV<sub>3</sub>O<sub>8</sub> (monoclinic s.g. *C2/m* [81]), and MgV<sub>2</sub>O<sub>4</sub> (cubic s.g. *Fd-3m* [82]) phases have been used as input for BVS calculation and results are presented in Figure 11.

In magnesium orthovanadate, Mg<sub>3</sub>V<sub>2</sub>O<sub>8</sub>, Mg<sup>2+</sup> occupies two types of octahedral sites, Mg1 and Mg2 crystallographic position, thus forming layers of edge-sharing Mg<sub>1</sub>O<sub>6</sub> and Mg<sub>2</sub>O<sub>6</sub> octahedra in ac-plane; the MgO<sub>n</sub> layers are separated by VIO<sub>4</sub> tetrahedrons, as depicted in Figure 11a. Although transport within the layer seems most probable, this is not the case, since there exists no continuous network of BVS isosurfaces in the structure of Mg<sub>3</sub>V<sub>2</sub>O<sub>8</sub>; there are only isolated “islands” of possible Mg<sup>2+</sup> occurrence, including both Mg1 and Mg2 sites, and one additional interstitial position (encircled with dashed line in Figure 11b). This suggests that magnesium ions remain firmly trapped in their respective positions, making the structure more/less inactive for reversible magnesium extraction, as confirmed by electrochemical measurements (Figure S4b, Supplementary Materials).

In the second investigated structure, which is beta phase MgV<sub>3</sub>O<sub>8</sub>, magnesium occupies an octahedral position with symmetry: 1 (denoted as Mg1), which it randomly shares with one V<sup>4+</sup> ion; edge- and corner-shared Mg<sub>1</sub>O<sub>6</sub> octahedrons thus form layers normal to A-axis, which are pillared by V<sup>5+</sup>O<sub>4</sub> tetrahedrons and V<sup>5+</sup>O<sub>5</sub> hexahedrons, as presented in Figure 11c. The Mg<sup>2+</sup> diffusion within this structure is achieved dominantly through a set of intersected tunnels in ab-plane, as could be seen in Figure 11d. Note that Mg1 position is located outside of the planar tunnel network, suggesting that partial occupation of this position by V<sup>4+</sup> could not significantly affect migration of Mg<sup>2+</sup> ions.

In the third structure of interest, which is spinel MgV<sub>2</sub>O<sub>4</sub> (displayed in Figure 11e), Mg<sup>2+</sup> and V<sup>3+</sup> ion occupy one tetrahedral Mg1 and one octahedral V1 position, respectively. Mg<sub>1</sub>O<sub>4</sub> shares only corners with neighboring VIO<sub>6</sub> and has neither common corners nor edges with other Mg<sub>1</sub>O<sub>4</sub>. Still, for the applied BVS mismatch of ±0.1 v.u, Mg1 sites are interconnected through broad channels of BVS isosurfaces, thus providing an extensive

tunnel network for 3D migration of  $Mg^{2+}$  ions (Figure 11f,g). According to the insights into possible  $Mg^{2+}$  diffusion pathways of the three structures of the MgVO/C material, provided by BVS calculations, the  $Mg^{2+}$  ion conduction capabilities of the investigated phases decrease in order:  $MgV_2O_4 > MgV_3O_8 > Mg_3V_2O_8$ .

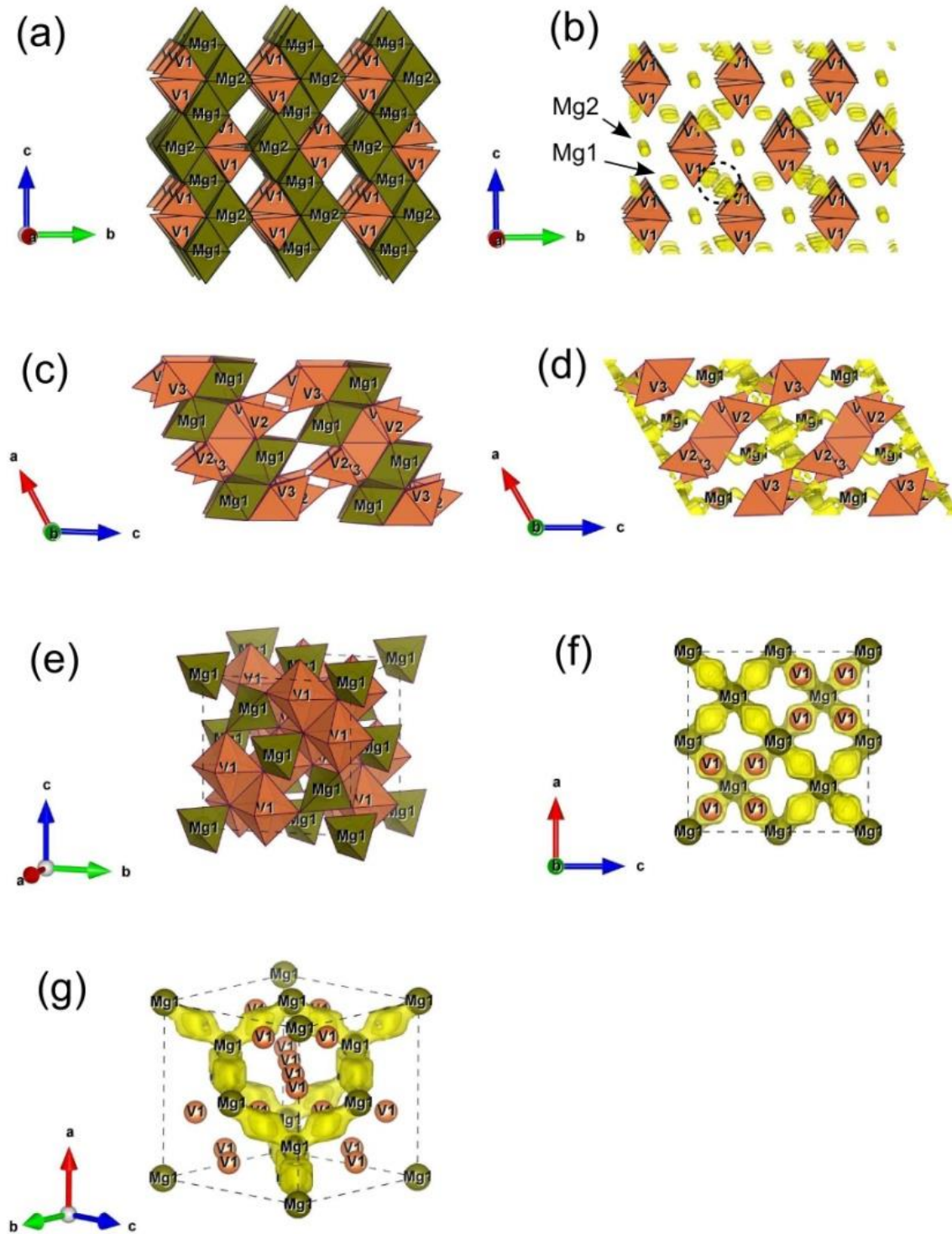


**Figure 11.** Models of migration pathways for  $Mg^{2+}$  ion obtained by BVS analysis of vanadate phase constituents of MgVO/C. Polyhedral representation of  $Mg_3V_2O_8$  (a) and BVS map within its structure (b); polyhedral representation of  $\beta$ - $MgV_3O_8$  (c) and BVS map within its structure (d); polyhedral representation of  $MgV_2O_4$  (e) and BVS map within its structure viewed from different directions (f,g). BVS volumes are defined by  $\pm 0.1$  v.u. mismatch from the valence +2 of Mg.



Further, if we combine results obtained via BVS analysis of all aforementioned vanadate phases, they can be classified with respect to  $\text{Mg}^{2+}$  ionic diffusion capabilities as follows: (1) the  $\text{MgV}_2\text{O}_4$  phases would fall into category of good  $\text{Mg}^{2+}$  ionic conductors; (2)  $\text{MgV}_3\text{O}_8$  as a medium conductor; (3)  $\text{Mg}_2\text{VO}_6$  as a poor conductor; while (4)  $\text{Mg}_3\text{V}_2\text{O}_8$  and  $\alpha\text{-Mg}_2\text{V}_2\text{O}_7$  structures have no potential for reversible magnesium extraction. These findings could serve as a solid basis for future development of cathodes among different magnesium vanadate materials.

### 3.5.2. Comparison of the MgVO/C Performance in the $\text{Mg}^{2+}$ , $\text{Al}^{3+}$ , and $\text{Li}^+$ Electrolytes

For comparison purposes, the MgVO/C material was additionally electrochemically tested in 1M  $\text{Al}(\text{NO}_3)_3$  and 6M  $\text{LiNO}_3$  by cyclic voltammetry measurements. Some similarities in the behavior of the CVs recorded in different media can be observed (Figures 9 and 12). In the case of the  $\text{Al}(\text{NO}_3)_3$  electrolyte, insertion/deinsertion of  $\text{Al}^{3+}$  ions occurred, while the values of current grew up to the 21st cycle, after which a decline in the current values took place in a manner similar to that of MgVO-LT (Figure 12a), resulting from partial damage of the electrode material, as explained in the previous part. However, the maximum current density achieved in the  $\text{Al}(\text{NO}_3)_3$  is about twice lower than that achieved in the  $\text{Mg}(\text{NO}_3)_2$  (Figure 12c). In the case of  $\text{LiNO}_3$  electrolyte and insertion/deinsertion of  $\text{Li}^+$  ions, growth of the current was observed up to the 13th cycle (Figure 12b), while the maximum current density was about 35% lower than that in  $\text{Mg}(\text{NO}_3)_2$  (Figure 12c). Higher stability of the Mg-V-O materials in  $\text{Mg}^{2+}$  electrolyte than in the other ones could, to a large extent, result from the higher tendency of  $\text{Mg}^{2+}$  ions to occupy the sites around apical oxygen atoms than that of the  $\text{Al}^{3+}$  and  $\text{Li}^+$  ions, leading to redistribution of charge and reduced tension of crystal lattices [40]. Certain changes in the shape of the CVs in  $\text{Al}(\text{NO}_3)_3$  and  $\text{LiNO}_3$  observed with the progress of cycling suggested that some of the inserted  $\text{Al}^{3+}$  and  $\text{Li}^+$  ions could not be completely extracted from the starting MgVO/C structure [83], which could also include an irreversible phase transition during the electrochemical cycling [46].

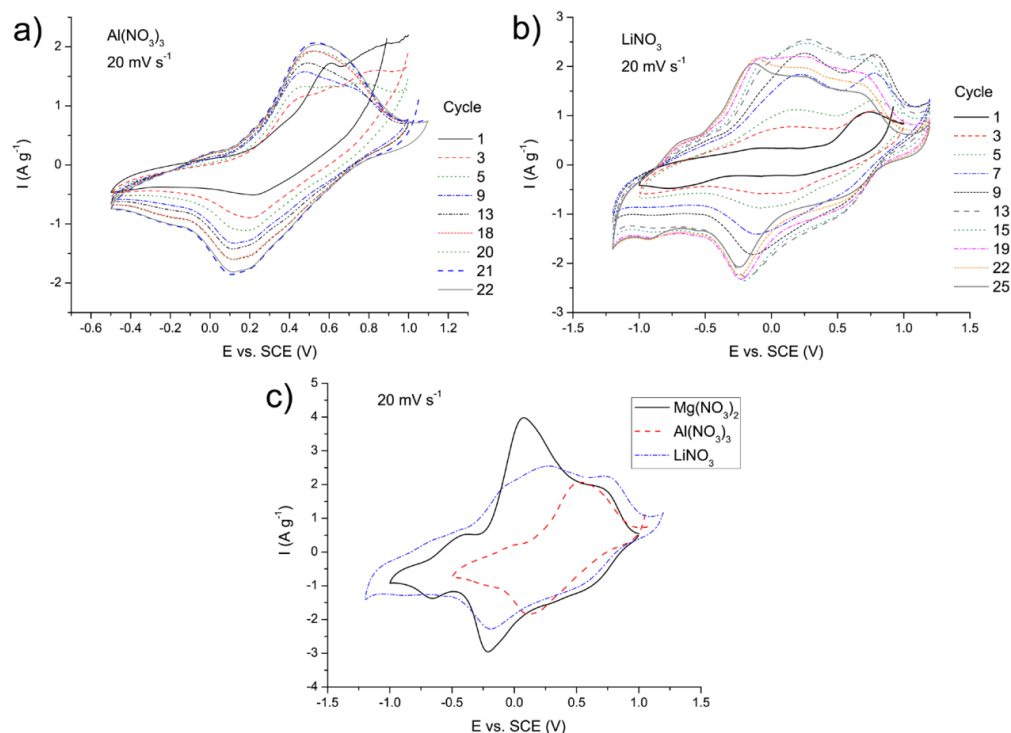


**Figure 12.** Cyclic voltammograms of the MgVO/C recorded at  $20 \text{ mV s}^{-1}$  in 1M  $\text{Al}(\text{NO}_3)_3$  (a) and 6M  $\text{LiNO}_3$  (b), showing together the highest currents achieved in three different media (Mg, Al, and Li nitrate) (c).

#### 4. Conclusions

MgVO materials of various structures, synthesized by simple preparation route including precipitation followed by thermal annealing, were studied as potential cathode materials for rechargeable aqueous magnesium ion batteries.

Redox behavior of the examined materials was shown to be complex and dependent on the structure (phase composition). Multiphase oxide systems (MgVO-LT and MgVO/C) exhibited better  $Mg^{2+}$  insertion/deinsertion performances than the single-phase ones ( $MgV_2O_6$  and  $Mg_2V_2O_7$ ). It was suggested that some kind of synergistic effect among different phases of MgVO-LT is possible during the electrochemical processes, in spite of the slow  $Mg^{2+}$  ion diffusion in the  $MgV_2O_6$  and  $Mg_2V_2O_7$  phases.

To improve redox activity of the  $MgV_2O_6$  phase, carbon was integrated with the MgVO-HT material by sucrose-assisted thermal treatment, yielding MgVO/C. Carbon addition was shown to be an effective dual strategy for enhancing electrochemical performance of the studied MgVO materials. Role of carbon included improvement of electrical conductivity of the magnesium vanadium oxide sample as well as the phase transformation into phases with better  $Mg^{2+}$  diffusion properties than those of the  $MgV_2O_6$  phase. Better electrochemical activity for insertion/deinsertion of metal ions and higher stability of MgVO/C was observed in the  $Mg^{2+}$  electrolyte compared with the  $Al^{3+}$  and  $Li^+$  ones, probably because of the greater tendency of  $Mg^{2+}$  ions to occupy the sites around apical oxygen atoms than that of the  $Al^{3+}$  and  $Li^+$ , and resulting reduced tension of crystal lattices in the case of  $Mg^{2+}$  electrolyte. All this makes the magnesium vanadium oxide materials promising for further development with a view to their application in rechargeable aqueous magnesium ion batteries.

**Supplementary Materials:** The following supporting information can be downloaded at: <https://www.mdpi.com/article/10.3390/nano12162767/s1>, Figure S1: SEM micrographs of MgVO-LT at different positions and magnifications; Figure S2: Cyclic voltammograms of MgVO-HT in 1M  $Al(NO_3)_3$ , at 20  $mV s^{-1}$ ; Figure S3: Raman spectra of the MgVO-LT electrode material acquired at different spots, before and after electrochemical treatments in  $Mg(NO_3)_2$  and  $Al(NO_3)_3$ ; Figure S4: Cyclic voltammograms of  $Mg_2V_2O_7$  (a) and  $Mg_3V_2O_8$  (b) materials in 3 M  $Mg(NO_3)_2$ , at 20  $mV s^{-1}$ ; Table S1: Assignment of the FTIR and Raman spectral bands of the MgVO precursor material; Table S2: Comparative electrochemical properties of VO-based oxides in Mg-containing aqueous solutions.

**Author Contributions:** Investigation, M.M.V., M.M., T.P. and D.B.-B.; Conceptualization M.M.V. and M.J.V.; Methodology M.M.V., M.M., D.B.-B. and M.J.V.; Writing-original draft, M.M.V. and M.M.; Supervision M.J.V.; project administration, M.J.V.; Writing-review&editing, M.J.V. All authors have read and agreed to the published version of the manuscript.

**Funding:** This research was supported by the Science Fund of the Republic of Serbia, under the project PROMIS #6062667 (HISUPERBAT). The Ministry of Education, Science and Technological Development of the Republic of Serbia (contract No. 451-03-68/2022-14/200146 and No. 451-03-68/2022-14/200175) also support this work.

**Data Availability Statement:** Not applicable.

**Conflicts of Interest:** The authors declare no conflict of interest.

#### References

1. Li, M.; Lu, J.; Chen, Z.; Amine, K. 30 Years of lithium-ion batteries. *Adv. Mater.* **2018**, *30*, 1800561. [[CrossRef](#)] [[PubMed](#)]
2. Zhu, L.; Bao, C.; Xie, L.; Yang, X.; Cao, X. Review of synthesis and structural optimization of  $LiNi_{1/3}Co_{1/3}Mn_{1/3}O_2$  cathode materials for lithium-ion batteries applications. *J. Alloy. Compd.* **2020**, *831*, 154864. [[CrossRef](#)]
3. Wen, J.; Yu, Y.; Chen, C. A review on lithium-ion batteries safety issues: Existing problems and possible solutions. *Mater. Express* **2012**, *2*, 197–212. [[CrossRef](#)]
4. Heubner, C.; Nikolowski, K.; Reuber, S.; Schneider, M.; Wolter, M.; Michaelis, A. Recent insights into rate performance limitations of Li-ion batteries. *Batter. Supercaps* **2021**, *4*, 268–285. [[CrossRef](#)]
5. Li, L.; Lu, Y.; Zhang, Q.; Zhao, S.; Hu, Z.; Chou, S.L. Recent progress on layered cathode materials for nonaqueous rechargeable magnesium batteries. *Small* **2019**, *17*, 1902767. [[CrossRef](#)] [[PubMed](#)]

6. Liu, Q.; Hu, Z.; Chen, M.; Zou, C.; Jin, H.; Wang, S.; Chou, S.L.; Dou, S.X. Recent progress of layered transition metal oxide cathodes for sodium-ion batteries. *Small* **2019**, *15*, 1805381. [[CrossRef](#)]
7. Zhang, Y.; Liu, S.; Ji, Y.; Ma, J.; Yu, H. Emerging nonaqueous aluminum-ion batteries: Challenges, status, and perspectives. *Adv. Mater.* **2018**, *30*, 1706310. [[CrossRef](#)]
8. Zhang, N.; Dong, Y.; Jia, M.; Bian, X.; Wang, Y.; Qiu, M.; Xu, J.; Liu, Y.; Jiao, L.; Cheng, F. Rechargeable aqueous Zn–V<sub>2</sub>O<sub>5</sub> battery with high energy density and long cycle life. *ACS Energy Lett.* **2018**, *3*, 1366–1372. [[CrossRef](#)]
9. Walter, M.; Kovalenko, M.V.; Kravchuk, K.V. Challenges and benefits of post-lithium-ion batteries. *New J. Chem.* **2020**, *44*, 1677–1683. [[CrossRef](#)]
10. Pan, W.; Liu, C.; Wang, M.-Y.; Zhang, Z.-J.; Yan, X.-Y.; Yang, S.-C.; Liu, X.-H.; Wang, Y.-F.; Leung, D. Non-aqueous Al-ion batteries: Cathode materials and corresponding underlying ion storage mechanisms. *Rare Met.* **2022**, *41*, 762–774. [[CrossRef](#)]
11. Song, Y.; Chen, Y.; Wang, Z.; Zhao, W.; Qin, C.; Yu, H.; Wang, X.; Bakenov, Z.; Zhang, Y. Defective ZnOx@porous carbon nanofiber network inducing dendrite-free zinc plating as zinc metal anode for high-performance aqueous rechargeable Zn/Na<sub>4</sub>Mn<sub>9</sub>O<sub>18</sub> battery based on hybrid electrolyte. *J. Power Sources* **2022**, *518*, 230761. [[CrossRef](#)]
12. Karapidakis, E.; Vernardou, D. Progress on V<sub>2</sub>O<sub>5</sub> cathodes for multivalent aqueous batteries. *Materials* **2021**, *14*, 2310. [[CrossRef](#)] [[PubMed](#)]
13. Lan, T.; Tsai, C.-L.; Tietz, F.; Wei, X.-K.; Heggen, M.; Dunin-Borkowski, R.E.; Wang, R.; Xiao, Y.; Ma, Q.; Guillon, O. Room-temperature all-solid-state sodium batteries with robust ceramic interface between rigid electrolyte and electrode materials. *Nano Energy* **2019**, *65*, 104040. [[CrossRef](#)]
14. Legeein, C.; Morgan, B.; Fayon, F.; Koketsu, T.; Ma, J.; Body, M.; Sarou-Kanian, V.; Wei, X.; Heggen, M.; Borkiewicz, O.; et al. Atomic Insights into Aluminium-Ion Insertion in Defective Anatase for Batteries. *Angew. Chem.* **2020**, *59*, 19247. [[CrossRef](#)]
15. Yan, C.; Lv, C.; Wang, L.; Cui, W.; Zhang, L.; Dinh, K.N.; Tan, H.; Wu, C.; Wu, T.; Ren, Y.; et al. Architecting a stable high-energy aqueous Al-ion battery. *J. Am. Chem. Soc.* **2020**, *142*, 15295–15304. [[CrossRef](#)] [[PubMed](#)]
16. Wang, Z.; Zhou, M.; Qin, L.; Chen, M.; Chen, Z.; Guo, S.; Wang, L.; Fang, G.; Liang, S. Simultaneous regulation of cations and anions in an electrolyte for high-capacity, high-stability aqueous zinc–vanadium batteries. *Escience* **2022**, *2*, 209–218. [[CrossRef](#)]
17. Novak, P.; Desilvestro, J. Electrochemical insertion of magnesium in metal oxides and sulfides from aprotic electrolytes. *J. Electrochem. Soc.* **1993**, *140*, 140–144. [[CrossRef](#)]
18. Zhang, Y.; Geng, H.; Wei, W.; Ma, J.; Chen, V.; Li, C.C. Challenges and recent progress in the design of advanced electrode materials for rechargeable Mg batteries. *Energy Storage Mater.* **2019**, *20*, 118–138. [[CrossRef](#)]
19. Wang, C.; Zhang, L.; Zhang, Z.; Zhao, R.; Zhao, D.; Ma, R.; Yin, L. Layered materials for supercapacitors and batteries: Applications and challenges. *Prog. Mater. Sci.* **2021**, *118*, 100763. [[CrossRef](#)]
20. Zhang, Z.; Zhang, X.; Zhao, X.; Yao, S.; Chen, A.; Zhou, Z. Computational screening of layered materials for multivalent ion batteries. *ACS Omega* **2019**, *4*, 7822–7828. [[CrossRef](#)]
21. Zhu, Y.; Huang, G.; Yin, J.; Lei, Y.; Emwas, A.H.; Yu, X.; Mohammed, O.F.; Alshareef, H.N. Hydrated Mg<sub>x</sub>V<sub>5</sub>O<sub>12</sub> cathode with improved Mg<sup>2+</sup> storage performance. *Adv. Energy Mater.* **2020**, *10*, 2002128. [[CrossRef](#)]
22. Liu, Z.; Qin, L.; Cao, X.; Zhou, J.; Pan, A.; Fang, G.; Wang, S.; Liang, S. Ion migration and defect effect of electrode materials in multivalent-ion batteries. *Prog. Mater. Sci.* **2022**, *125*, 100911. [[CrossRef](#)]
23. Mao, M.; Gao, T.; Hou, S.; Chunsheng, W. A critical review of cathodes for rechargeable Mg batteries. *Chem. Soc. Rev.* **2018**, *47*, 8804. [[CrossRef](#)] [[PubMed](#)]
24. Xiao, R.; Xie, J.; Luo, T.; Huang, L.; Zhou, Y.; Yu, D.; Chen, C.; Liu, Y. Phase transformation and diffusion kinetics of V<sub>2</sub>O<sub>5</sub> electrode in rechargeable Li and Mg batteries: A first-principle study. *J. Phys. Chem. C* **2018**, *122*, 1513–1521. [[CrossRef](#)]
25. Kaveevivitchai, W.; Jacobson, A.J. High capacity rechargeable magnesium-ion batteries based on a microporous molybdenum-vanadium oxide cathode. *Chem. Mater.* **2016**, *28*, 4593–4601. [[CrossRef](#)]
26. Kim, R.H.; Kim, J.S.; Kim, H.J.; Chang, W.S.; Han, D.W.; Lee, S.S.; Doo, S.G. Highly reduced VO<sub>x</sub> nanotube cathode materials with ultra-high capacity for magnesium ion batteries. *J. Mater. Chem. A* **2014**, *2*, 20636–20641. [[CrossRef](#)]
27. Johnson, I.D.; Stapleton, N.; Nolis, G.; Bauer, D.; Parajuli, P.; Yoo, H.D.; Yin, L.; Ingram, B.J.; Klie, R.F.; Lapidus, S.; et al. Control of crystal size tailors the electrochemical performance of α-V<sub>2</sub>O<sub>5</sub> as a Mg<sup>2+</sup> intercalation host. *Nanoscale* **2021**, *13*, 10081–10091. [[CrossRef](#)] [[PubMed](#)]
28. Hu, L.; Jokisaari, J.R.; Kwon, B.J.; Yin, L.; Kim, S.; Park, H.; Lapidus, S.H.; Klie, R.F.; Key, B.; Zapol, P.; et al. High capacity for Mg<sup>2+</sup> deintercalation in spinel vanadium oxide nanocrystals. *ACS Energy Lett.* **2020**, *5*, 2721–2727. [[CrossRef](#)]
29. Xu, Y.; Deng, X.; Li, Q.; Zhang, G.; Xiong, F.; Tan, S.; Wei, Q.; Lu, J.; Li, J.; An, Q.; et al. Vanadium oxide pillared by interlayer Mg<sup>2+</sup> ions and water as ultralong-life cathodes for magnesium-ion batteries. *Chem* **2019**, *5*, 1194–1209. [[CrossRef](#)]
30. Du, X.; Huang, G.; Qin, Y.; Wang, L. Solvothermal synthesis of GO/V<sub>2</sub>O<sub>5</sub> composites as a cathode material for rechargeable magnesium batteries. *RSC Adv.* **2015**, *5*, 76352–76355. [[CrossRef](#)]
31. Inamoto, M.; Kurihara, H.; Yajima, T. Electrode performance of vanadium pentoxide xerogel prepared by microwave irradiation as an active cathode material for rechargeable magnesium batteries. *Electrochemistry* **2012**, *80*, 421–422. [[CrossRef](#)]
32. Yin, J.; Pelliccione, C.J.; Lee, S.H.; Takeuchi, E.S.; Takeuchi, K.J.; Marschilok, A.C. Communication—Sol-gel synthesized magnesium vanadium oxide, Mg<sub>x</sub>V<sub>2</sub>O<sub>5</sub>·nH<sub>2</sub>O: The role of structural Mg<sup>2+</sup> on battery performance. *J. Electrochem. Soc.* **2016**, *163*, A1941–A1943. [[CrossRef](#)]
33. Sun, J.Z. Study of MgV<sub>2</sub>O<sub>6</sub> as cathode material for secondary magnesium batteries. *Asian J. Chem.* **2011**, *23*, 1399–1400.

34. Inamoto, M.; Kurihara, H.; Yajima, T. Vanadium pentoxide-based composite synthesized using microwave water plasma for cathode material in rechargeable magnesium batteries. *Materials* **2013**, *6*, 4514–4522. [[CrossRef](#)] [[PubMed](#)]
35. Jiao, L.F.; Yuan, H.T.; Si, Y.C.; Wang, Y.J.; Wang, Y.M. Synthesis of Cu<sub>0.1</sub>-doped vanadium oxide nanotubes and their application as cathode materials for rechargeable magnesium batteries. *Electrochem. Commun.* **2006**, *8*, 1041–1044. [[CrossRef](#)]
36. Demir-Cakan, R.; Palacín, M.R.; Croguennec, L. Rechargeable aqueous electrolyte batteries: From univalent to multivalent cation chemistry. *J. Mater. Chem. A* **2019**, *7*, 20519–20539. [[CrossRef](#)]
37. Chao, D.; Zhou, W.; Xie, F.; Ye, C.; Li, H.; Jaroniec, M.; Qiao, S.Z. Roadmap for advanced aqueous batteries: From design of materials to applications. *Sci. Adv.* **2020**, *6*, eaba4098. [[CrossRef](#)]
38. Wang, F.; Fan, X.; Gao, T.; Sun, W.; Ma, Z.; Yang, C.; Han, F.; Xu, K.; Wang, C. High-voltage aqueous magnesium ion batteries. *ACS Central Sci.* **2017**, *3*, 1121–1128. [[CrossRef](#)]
39. Song, J.; Sahadeo, E.; Noked, M.; Lee, S.B. Mapping the challenges of magnesium battery. *J. Phys. Chem. Lett.* **2016**, *7*, 1736–1749. [[CrossRef](#)]
40. Vujković, M.; Pašti, I.; Simatović, I.S.; Šljukić, B.; Milenković, M.; Mentus, S. The influence of intercalated ions on cyclic stability of V<sub>2</sub>O<sub>5</sub>/graphite composite in aqueous electrolytic solutions: Experimental and theoretical approach. *Electrochim. Acta* **2015**, *176*, 130–140. [[CrossRef](#)]
41. Vujković, M.J.; Mladenović, D.; Milović, M.; Petrović, T.; Bogdanović, D.B.; Paunković, B.Š.; Mentus, S. Sodium-pillared vanadium oxides as next-gen materials: Does co-inserted water control the cyclic stability of vanadates in an aqueous electrolyte? *Electrochim. Acta* **2022**, *425*, 140603. [[CrossRef](#)]
42. Charles, D.S.; Feyngenson, M.; Page, K.; Neuefeind, J.; Xu, W.; Teng, X. Structural water engaged disordered vanadium oxide nanosheets for high capacity aqueous potassium-ion storage. *Nat. Commun.* **2017**, *8*, 15520. [[CrossRef](#)] [[PubMed](#)]
43. Wan, F.; Zhang, L.; Dai, X.; Wang, X.; Niu, Z.; Chen, J. Aqueous rechargeable zinc/sodium vanadate batteries with enhanced performance from simultaneous insertion of dual carriers. *Nat. Commun.* **2018**, *9*, 1656. [[CrossRef](#)]
44. Yan, M.; He, P.; Chen, Y.; Wang, S.; Wei, Q.; Zhao, K.; Xu, X.; An, Q.; Shuang, Y.; Shao, Y.; et al. Water-lubricated intercalation in V<sub>2</sub>O<sub>5</sub>-nH<sub>2</sub>O for high-capacity and high-rate aqueous rechargeable zinc batteries. *Adv. Mater.* **2018**, *30*, 1703725. [[CrossRef](#)]
45. Kundu, D.; Adams, B.D.; Duffort, V.; Vajargah, S.H.; Nazar, L.F. A high-capacity and long-life aqueous rechargeable zinc battery using a metal oxide intercalation cathode. *Nat. Energy* **2016**, *1*, 16119. [[CrossRef](#)]
46. Wang, L.; Huang, K.W.; Chen, J.; Zheng, J. Ultralong cycle stability of aqueous zinc-ion batteries with zinc vanadium oxide cathodes. *Sci. Adv.* **2019**, *5*, eaax4279. [[CrossRef](#)]
47. Dong, S.; Shin, W.; Jiang, H.; Wu, X.; Li, Z.; Holoubek, J.; Stickle, W.F.; Key, B.; Liu, C.; Lu, J.; et al. Ultra-fast NH<sub>4</sub><sup>+</sup> storage: Strong H bonding between NH<sub>4</sub><sup>+</sup> and bi-layered V<sub>2</sub>O<sub>5</sub>. *Chem* **2019**, *5*, 1537–1551. [[CrossRef](#)]
48. Liu, Y.; Wu, X. Review of vanadium-based electrode materials for rechargeable aqueous zinc ion batteries. *J. Energy Chem.* **2021**, *56*, 223–237. [[CrossRef](#)]
49. Jo, J.H.; Sun, Y.K.; Myung, S.T. Hollandite-type Al-doped VO<sub>1.52</sub>(OH)<sub>0.77</sub> as a zinc ion insertion host material. *J. Mater. Chem. A* **2017**, *5*, 8367–8375. [[CrossRef](#)]
50. González, J.R.; Nacimiento, F.; Cabello, M.; Alcántara, R.; Lavela, P.; Tirado, J.L. Reversible intercalation of aluminium into vanadium pentoxide xerogel for aqueous rechargeable batteries. *RSC Adv.* **2016**, *6*, 62157–62164. [[CrossRef](#)]
51. Soenen, V.; Herrmann, J.M.; Volta, J.C. In situ electrical characterization of magnesium vanadate reference phases (meta-MgV<sub>2</sub>O<sub>6</sub>, pyro-Mg<sub>2</sub>V<sub>2</sub>O<sub>7</sub>, and ortho-Mg<sub>3</sub>V<sub>2</sub>O<sub>8</sub>) used in oxidative dehydrogenation of propane to propene. *J. Catal.* **1996**, *159*, 410–417. [[CrossRef](#)]
52. Rybarczyk, P.; Berndt, H.; Radnik, J.; Pohl, M.M.; Buyevskaya, O.; Baerns, M.; Brückner, A. The structure of active sites in Me–V–O catalysts (Me = Mg, Zn, Pb) and its influence on the catalytic performance in the oxidative dehydrogenation (ODH) of propane. *J. Catal.* **2001**, *202*, 45–58. [[CrossRef](#)]
53. ICSD. *Inorganic Crystals Structure Database*; FIZ Karlsruhe: Eggenstein-Leopoldshafen, Germany, 2014.
54. Scherrer, P. Bestimmung der gröÙe und der inneren struktur von kolloidteilchen mittels röntgenstrahlen, Nachrichten von der Gesellschaft der Wissenschaften zu Göttingen. *Abh. Akad. Wiss. Gött. Math.-Phys. Kl.* **1918**, *2*, 98–100.
55. Sale, M.; Avdeev, M. 3DBVSMAPPER: A program for automatically generating bond-valence sum landscapes. *J. Appl. Crystallogr.* **2012**, *45*, 1054–1056. [[CrossRef](#)]
56. Adams, S. Practical Considerations in Determining Bond Valence Parameters. In *Bond Valence*; Brown, I.D., Poeppelmeier, K.R., Eds.; Springer: Berlin/Heidelberg, Germany, 2014; pp. 91–128.
57. Mojet, B.L.; Ebbesen, S.D.; Lefferts, L. Light at the interface: The potential of attenuated total reflection infrared spectroscopy for understanding heterogeneous catalysis in water. *Chem. Soc. Rev.* **2010**, *39*, 4643–4655. [[CrossRef](#)]
58. Hanuza, J.; Jezowska-Trzebiatowska, B.; Oganowski, W. Structure of the active layer and catalytic mechanism of the V<sub>2</sub>O<sub>5</sub>/MgO catalysts in the oxidative dehydrogenation of ethylbenzene to styrene. *J. Mol. Catal.* **1985**, *29*, 109–143. [[CrossRef](#)]
59. Gao, X.; Ruiz, P.; Xin, Q.; Guo, X.; Delmon, B. Effect of coexistence of magnesium vanadate phases in the selective oxidation of propane to propene. *J. Catal.* **1994**, *148*, 56–67. [[CrossRef](#)]
60. Corma, A.; Nieto, J.M.L.; Paredes, N. Influence of the preparation methods of V-Mg-O catalysts on their catalytic properties for the oxidative dehydrogenation of propane. *J. Catal.* **1993**, *144*, 425–438. [[CrossRef](#)]
61. Jin, M.; Cheng, Z.M. Oxidative dehydrogenation of cyclohexane to cyclohexene over Mg-V-O catalysts. *Catal. Lett.* **2009**, *131*, 266–278. [[CrossRef](#)]

62. Heyns, A.M.; Venter, M.W.; Range, K.J. The vibrational spectra of  $\text{NH}_4\text{VO}_3$  at elevated temperatures and pressures. *Z. Naturforsch.* **1987**, *42b*, 843–852. [[CrossRef](#)]
63. Rahman, M.A.; Sarker, M.A.R. Synthesis, characterization and physical properties of high quality  $\text{MgV}_2\text{O}_6$  crystals by solid-state reaction and ab-initio methods. *J. Alloy. Compd.* **2019**, *797*, 630–639. [[CrossRef](#)]
64. Imamura, D.; Miyayama, M. Characterization of magnesium-intercalated  $\text{V}_2\text{O}_5$ /carbon composites. *Solid State Ion.* **2003**, *161*, 173–180. [[CrossRef](#)]
65. Keen, O.S.; Love, N.G.; Linden, K.G. Nitrate photochemistry in the context of water reclamation. In *Water Reclamation and Sustainability*; Ahuja, S., Ed.; Elsevier: Amsterdam, The Netherlands, 2014; pp. 229–246.
66. Li, P.; Zhou, W.; Wang, X.; Zhang, Y.; Umezawa, N.; Abe, H.; Ye, J.; Wang, D. Effects of cation concentration on photocatalytic performance over magnesium vanadates. *APL Mater.* **2015**, *3*, 104405. [[CrossRef](#)]
67. Choi, N.H.; Kwon, S.; Kim, H. Analysis of the oxidation of the V(II) by dissolved oxygen using UV-visible spectrophotometry in a vanadium redox flow battery. *J. Electrochem. Soc.* **2013**, *160*, A973–A979. [[CrossRef](#)]
68. Venkatesan, A.; Chandar, N.R.K.; Pradeeswari, K.; Pandi, P.; Kandasamy, A.; Kumar, R.M.; Jayavel, R. Influence of Al doping on structural, luminescence and electrochemical properties of  $\text{V}_2\text{O}_5$  nanostructures synthesized via non-hydrolytic sol-gel technique. *Mater. Res. Express.* **2019**, *6*, 015017. [[CrossRef](#)]
69. Zhang, W.; Zuo, C.; Tang, C.; Tang, W.; Lan, B.; Fu, X.; Dong, S.; Luo, P. The current developments and perspectives of  $\text{V}_2\text{O}_5$  as cathode for rechargeable aqueous zinc-ion batteries. *Energy Technol.* **2021**, *9*, 2000789. [[CrossRef](#)]
70. Rastgoo-Deylami, M.; Chae, M.S.; Hong, S.T.  $\text{H}_2\text{V}_3\text{O}_8$  as a high energy cathode material for nonaqueous magnesium-ion batteries. *Chem. Mater.* **2018**, *30*, 7464–7472. [[CrossRef](#)]
71. Ng, H.N.; Calvo, C. Crystal Structure of and Electron Spin Resonance of  $\text{Mn}^{2+}$  in  $\text{MgV}_2\text{O}_6$ . *Can. J. Chem.* **1972**, *50*, 3619–3624. [[CrossRef](#)]
72. Shklover, V.; Haibach, T.; Ried, F.; Nesper, R.; Novák, P. Crystal Structure of the Product of  $\text{Mg}^{2+}$  Insertion into  $\text{V}_2\text{O}_5$  Single Crystals. *J. Solid State Chem.* **1996**, *123*, 317–323. [[CrossRef](#)]
73. Nielsen, U.G.; Jakobsen, H.J.; Skibsted, J.; Norby, P. Crystal structure of  $\alpha\text{-Mg}_2\text{V}_2\text{O}_7$  from synchrotron X-ray powder diffraction and characterization by  $^{51}\text{V}$  MAS NMR spectroscopy. *J. Chem. Soc. Dalton Trans.* **2001**, *21*, 3214–3218. [[CrossRef](#)]
74. Sault, A.G.; Mudd, J.E.; Miller, J.E.; Ruffner, J.A.; Rodriguez, M.A.; Tissot, R.G. *Thin Film Models of Magnesium Orthovanadate Catalysts for Oxidative Dehydrogenation*; Sandia Report SAND2000-3157, Unlimited Release; Sandia National Laboratories: Albuquerque, NM, USA, 2001.
75. Fang, G.; Wang, Q.; Zhou, J.; Lei, Y.; Chen, Z.; Wang, Z.; Pan, A.; Liang, S. Metal organic framework-templated synthesis of bimetallic selenides with rich phase boundaries for sodium-ion storage and oxygen evolution reaction. *ACS Nano* **2019**, *13*, 5635–5645. [[CrossRef](#)] [[PubMed](#)]
76. Tang, H.; Xu, N.; Pei, C.; Xiong, F.; Tan, S.; Luo, W.; An, Q.; Mai, L.  $\text{H}_2\text{V}_3\text{O}_8$  nanowires as high-capacity cathode materials for magnesium-based battery. *ACS Appl. Mater. Interfaces* **2017**, *9*, 28667–28673. [[CrossRef](#)]
77. Drosos, C.; Jia, C.; Mathew, S.; Palgrave, R.G.; Moss, B.; Kafizas, A.; Vernardou, D. Aerosol-assisted chemical vapor deposition of  $\text{V}_2\text{O}_5$  cathodes with high rate capabilities for magnesium-ion batteries. *J. Power Sources* **2018**, *384*, 355–359. [[CrossRef](#)]
78. Drosos, C.; Moss, B.; Kafizas, A.; Vernardou, D.  $\text{V}_2\text{O}_5$  as magnesium cathode material with extended cyclic stability. *J. Electrochem. Sci. Eng.* **2020**, *10*, 257–262. [[CrossRef](#)]
79. Zhang, H.; Ye, K.; Zhu, K.; Cang, R.; Yan, J.; Cheng, K.; Wang, G.; Cao, D. High-energy-density aqueous magnesium-ion battery based on a carbon-coated  $\text{FeVO}_4$  anode and a Mg-OMS-1 cathode. *Chem. Eur. J.* **2017**, *23*, 17118–17126. [[CrossRef](#)]
80. Krishnamachari, N.; Calvo, C. Refinement of the Structure of  $\text{Mg}_3(\text{VO}_4)_2$ . *Can. J. Chem.* **1971**, *49*, 1629–1637. [[CrossRef](#)]
81. Saux, M.; Galy, J. Structure cristalline de  $\text{MgV}_3\text{O}_8$  beta. *Comptes Rendus Hebd. Seances Acad. Sci.* **1973**, *276*, 81–84.
82. Reuter, B.; Aust, R.; Colsmann, G.; Neuwald, C. Über Oxidssysteme mit Übergangsmetallionen in verschiedenen Oxydationsstufen. XIX. Darstellung und Eigenschaften Vanadium(II)-haltiger und damit n-leitender Vanadium(III)-Spinelle. *Z. Für Anorg. Allg. Chem.* **1983**, *500*, 188–198. [[CrossRef](#)]
83. Xu, D.; Wang, H.; Li, F.; Guan, Z.; Wang, R.; He, B.; Gong, Y.; Hu, X. Conformal conducting polymer shells on  $\text{V}_2\text{O}_5$  nanosheet arrays as a high-rate and stable zinc-ion battery cathode. *Adv. Mater. Interfaces* **2019**, *6*, 1801506. [[CrossRef](#)]